IMPLEMENTATION OF DOWN-HOLE GEOPHYSICAL TESTING FOR ROCK SOCKETS

FINAL REPORT

Sponsored by the Florida Department of Transportation Research Center
Contract Number BDV31-977-33

Dr. Dennis R. Hiltunen, P.E.
Principal Investigator

Dr. Jian Zou

DEPARTMENT OF CIVIL & COASTAL ENGINEERING
UNIVERSITY OF FLORIDA

February 2020

DISCLAIMER

The opinions, findings, and conclusions expressed in this publication are those of the authors and not necessarily those of the State of Florida Department of Transportation.

Prepared in cooperation with the State of Florida Department of Transportation.

SI* (MODERN METRIC) CONVERSION FACTORS

APPROXIMATE CONVERSIONS TO SI UNITS

SYMBOL	WHEN YOU KNOW	MULTIPLY BY	TO FIND	SYMBOL
		LENGTH		
in	inches	25.4	millimeters	mm
ft	feet	0.305	meters	m
yd	yards	0.914	meters	m
mi	miles	1.61	kilometers	km
		AREA		
in^2	square inches	645.2	square millimeters	mm^2
ft^2	square feet	0.093	square meters	m^2
yd^2	square yard	0.836	square meters	m^2
ac	acres	0.405	hectares	ha
mi^2	square miles	2.59	square kilometers	km^2
		VOLUME		
fl oz	fluid ounces	29.57	milliliters	mL
gal	gallons	3.785	liters	L
ft^3	cubic feet	0.028	cubic meters	m^3
yd^3	cubic yards	0.765	cubic meters	m^3
		NOTE: volumes greater than 1000 L shall be shown in m^3		
		MASS		
oz	ounces	28.35	grams	g
lb	pounds	0.454	kilograms	kg
T	short tons (2000 lb)	0.907	megagrams (or "metric ton")	Mg (or "t")
		TEMPERATURE (exact degrees)		
°F	Fahrenheit	5 (F-32)/9 or (F-32)/1.8	Celsius	°C
		ILLUMINATION		
fc	foot-candles	10.76	lux	lx
fl	foot-Lamberts	3.426	candela/m^2	cd/m^2
		FORCE and PRESSURE or STRESS		
lbf	poundforce	4.45	newtons	N
lbf/in^2	poundforce per square inch	6.89	kilopascals	kPa

APPROXIMATE CONVERSIONS FROM SI UNITS

SYMBOL	WHEN YOU KNOW	MULTIPLY BY	TO FIND	SYMBOL
		LENGTH		
mm	millimeters	0.039	inches	in
m	meters	3.28	feet	ft
m	meters	1.09	yards	yd
km	kilometers	0.621	miles	mi
		AREA		
mm^2	square millimeters	0.0016	square inches	in^2
m^2	square meters	10.764	square feet	ft^2
m^2	square meters	1.195	square yards	yd^2
ha	hectares	2.47	acres	ac
km^2	square kilometers	0.386	square miles	mi^2
		VOLUME		
mL	milliliters	0.034	fluid ounces	fl oz
L	liters	0.264	gallons	gal
m^3	cubic meters	35.314	cubic feet	ft^3
m^3	cubic meters	1.307	cubic yards	yd^3
		MASS		
g	grams	0.035	ounces	oz
kg	kilograms	2.202	pounds	lb
Mg (or "t")	megagrams (or "metric ton")	1.103	short tons (2000 lb)	T
		TEMPERATURE (exact degrees)		
°C	Celsius	1.8C+32	Fahrenheit	°F
		ILLUMINATION		
lx	lux	0.0929	foot-candles	fc
cd/m^2	candela/m^2	0.2919	foot-Lamberts	fl
		FORCE and PRESSURE or STRESS		
N	newtons	0.225	poundforce	lbf
kPa	kilopascals	0.145	poundforce per square inch	lbf/in^2

*SI is the symbol for the International System of Units. Appropriate rounding should be made to comply with Section 4 of ASTM E380.
(Revised March 2003)

TECHNICAL REPORT DOCUMENTATION PAGE

1. Report No.	2. Government Accession No.	3. Recipient's Catalog No.

4. Title and Subtitle	5. Report Date
Implementation of Down-Hole Geophysical Testing For Rock Sockets	February 2020
	6. Performing Organization Code
7. Author(s)	8. Performing Organization Report No.
Dennis R. Hiltunen and Jian Zou	
9. Performing Organization Name and Address	10. Work Unit No. (TRAIS)
Department of Civil and Coastal Engineering University of Florida 365 Weil Hall, P.O. Box 116580 Gainesville, FL 32611-6580	11. Contract or Grant No. BDV31-977-33
12. Sponsoring Agency Name and Address	13. Type of Report and Period Covered
Florida Department of Transportation 605 Suwannee Street, MS 30 Tallahassee, FL 32399	Final Report November 2014-February 2020
	14. Sponsoring Agency Code

15. Supplementary Notes

16. Abstract

The objective of the project was to produce a prototype instrument and software analysis system for conducting geophysical characterization of subsurface conditions from within a single borehole. In Task 1, Borehole Instrument, two piezoelectric sources were constructed, the first using high frequency piezocylinders and the second using a barrel stave flextensional transducer. A third low frequency source using pneumatic solenoids was also investigated. For receivers, a system was constructed for coupling accelerometers to the wall of a borehole, and an existing 3D string of geophones was also investigated. In Task 2, Inversion Software, an analysis software was developed to create an image of the material adjacent to a borehole using the measurements from the borehole instrument and full wave inversion (FWI) technology. In Task 3, Validation Experiments, we built three lab-scale experimental models in which to test our borehole instrument. These specimens were used extensively to investigate iterations of the instrument during development. We also used the boreholes at the Newberry field site to test both the low frequency solenoid source and the barrel stave source with the 3D geophone string. Overall, we have developed a working concept for a borehole instrument and analysis software for geophysical assessment of the material surrounding a geotechnical borehole. It has been demonstrated via both the piezoelectric and pneumatic solenoid sources and the accelerometer and geophone arrays that wavefields can be generated and measurably received within a single borehole. As well, we have shown using synthetically generated waveforms that a full waveform-based analysis software can image the material surrounding a borehole. Further equipment developments and both model and laboratory tests are warranted to help validate the new procedure.

17. Key Word	18. Distribution Statement
Down-hole testing, full waveform inversion, piezoelectric transducers, rock sockets, seismic methods	No Restrictions

19. Security Classif. (of this report)	20. Security Classif. (of this page)	21. No. of Pages	22. Price
Unclassified	Unclassified	68 Pages	

EXECUTIVE SUMMARY

The objective of the project was to produce a prototype instrument and software analysis system for conducting geophysical characterization of subsurface conditions from within a single borehole. In Task 1, Borehole Instrument, two piezoelectric sources were constructed, the first using high frequency piezocylinders and the second using a barrel stave flextensional transducer. A third low frequency source using pneumatic solenoids was also investigated. For receivers, a system was constructed for coupling accelerometers to the wall of a borehole, and an existing 3D string of geophones was also investigated. In Task 2, Inversion Software, an analysis software was developed to create an image of the material adjacent to a borehole using the measurements from the borehole instrument and full wave inversion (FWI) technology. In Task 3, Validation Experiments, we built three lab-scale experimental models in which to test our borehole instrument. These specimens were used extensively to investigate iterations of the instrument during development. We also used the boreholes at the Newberry field site to test both the low frequency solenoid source and the barrel stave source with the 3D geophone string. Overall, we have developed a working concept for a borehole instrument and analysis software for geophysical assessment of the material surrounding a geotechnical borehole. It has been demonstrated via both the piezoelectric and pneumatic solenoid sources and the accelerometer and geophone arrays that wavefields can be generated and measurably received within a single borehole. As well, we have shown using synthetically generated waveforms that a full waveform-based analysis software can image the material surrounding a borehole. Further equipment developments and both model and laboratory tests are warranted to help validate the new procedure.

TABLE OF CONTENTS

CHAPTER 1
INTRODUCTION

Decisions are required during drilled shaft construction that are influenced by the variability of rock formations within the vicinity of a drilled shaft's rock socket. Enhanced quality assurance testing could provide further information to assess the risk of this variability and would provide results to assist the engineer in making effective and efficient decisions. Existing site investigation tools (i.e., borings) have the limitation of only sampling a small volume of the soil and rock properties within the vicinity of the drilled shaft's rock socket. The proposed geophysical test offers the advantage of obtaining information over the entire volume of the rock socket. This is even more critical when larger diameter, non-redundant drilled shafts are utilized.

A previous research project, BDK75-977-51, Continuation of Down-Hole Geophysical Testing for Rock Sockets, showed that the concept of an improved geophysical method (placing a source and string of receivers down a single borehole) was successful in identifying the location and extent of known anomalies for several different numerical simulations. Based upon the design recommendations from that project, the equipment to perform actual field tests (in particular, the source for generating the required seismic waves) and the analysis software to reduce the raw data needed to be developed, enhanced, and piloted. The unanswered question was whether the concept developed in the previous project could be assembled into a hardware package that is practical for field use and whether the software to analyze the raw field data can accurately model rock properties around the borehole. This hardware-software system would be used in demonstrations on several sites throughout the state. These test sites will focus on the intended purpose of this test method – to assess the variability of rock formations and localized shear strength information of the rock within the vicinity of a drilled shaft's rock socket.

The objective of the proposed project was to produce a prototype instrument and software analysis system for conducting geophysical characterization of subsurface conditions from within a single borehole. The methodology was developed based on several small-scale applications and was demonstrated in a borehole at a site located in Newberry.

The project was conducted in the following three tasks that are described in Chapters 2-4: Task 1, Borehole Instrument, Task 2, Inversion Software, and Task 3, Validation Experiments. Chapter 5 presents the findings, conclusions, and recommendations from the project results.

CHAPTER 2
TASK 1: BOREHOLE INSTRUMENT

2.1 Introduction

The aim of Task 1 was to build a prototype instrument for geophysical characterization of a zone of rock around the periphery of a single borehole that is consistent with the successful numerical experiments completed in the previous research project. The two major components of the instrument are a source for generating seismic (mechanical) waves and a receiver array for capturing the wavefield generated by the source.

2.2 Source

Following the numerical experiments, it was desired that the source be a so-called monopole design that generates a ring-type loading around the circumference of a borehole. This loading scheme is consistent with the axisymmetric forward model used in inversion analysis of the numerical experiments. It would also be compatible with a fully 3D analysis system. Some initial ideas for the source included a "balloon-type" apparatus that is inflated quickly within the borehole to apply a uniformly distributed ring loading. The inflator could be driven by pneumatic or piezoelectric input. A mechanical cam-type device was also envisioned as an alternative. Based upon several sources of literature, a piezoelectric device appeared most preferable. Mechanical sources have typically been utilized for characterizing soil but have been found too slow for delivering a quick pulse required for characterizing rock. As demonstrated in the numerical experiments, it was also desirable that the source be able to create wavefields from multiple shot locations along the length of a fixed receiver array to improve resolution. As a minimum, the source should be capable of sliding along the borehole together with a receiver array in a so-called "land streamer" fashion.

2.2.1 High-Frequency Piezoelectric Cylinder

With the idea that a piezoelectric-based device appeared most feasible, a piezoelectric cylinder borehole source following the idea of Thill (1978) and shown in Figure 2-1 was followed. This implementation required a longer learning curve and time than originally anticipated. During the

first several months of experimentation at the start of the project, we successfully implemented a low-cost piezoelectric cylinder and power amplifier, which was our first experience with this type of equipment (Figure 2-2). Unfortunately, this first design did not have enough power (only 100 V and 33 mA RMS) and the cylinder chosen had a resonant frequency of 47 kHz (same piezocylinder as used in Olson CSL equipment), which we subsequently realized is far too high. Here we learned that each piezocylinder is designed to provide a maximum output centered narrowly on a resonant frequency and that the smaller the diameter of cylinder results in a higher resonance. The 47 kHz cylinder has a diameter of about 1 inch. We next purchased several alternative cylinder products with a range of resonant frequencies (from 14 kHz to 44 kHz) and diameters (from 1 inch to 3.5 inch) and a more powerful amplifier with higher output (350 V and 12 mA) (Figure 2-3). The cylinders worked well, but the second amplifier also proved inadequate. Here we learned that not only is more voltage required, but also higher current. A third power amplifier, a pulser device that supplies a high voltage (300 V) and high current (20 amp) over a short pulse, was then purchased and worked well in the Task 3: Validation Experiments (Figure 2-4). Unfortunately, each of the three power sources required 3+ months each to acquire since they are not items that are immediately in stock from equipment manufacturers that are all outside the United States. As a consequence, it took more than two years of equipment acquisition and subsequent implementation and evaluation in the validation experiments to arrive at a working concept for the piezoelectric cylinder borehole source.

With this working concept, we next constructed an inflatable canister (Figure 2-5) for repeatedly coupling a piezoelectric cylinder to the wall of a borehole following the idea of Thill (1978). The device houses a pair of piezocylinders wired in parallel inside an inflatable membrane. To inflate, the annulus between the cylinders and membrane is filled with castor oil that possesses appropriate dielectric properties for the cylinders to receive the high-output electric signal from the pulse amplifier while also being immersed in a fluid. The mechanical distortion of the cylinders upon firing is transferred through the oil and then out into the material surrounding the borehole. This canister system tested well in our small-scale experiments described in Chapter 4.

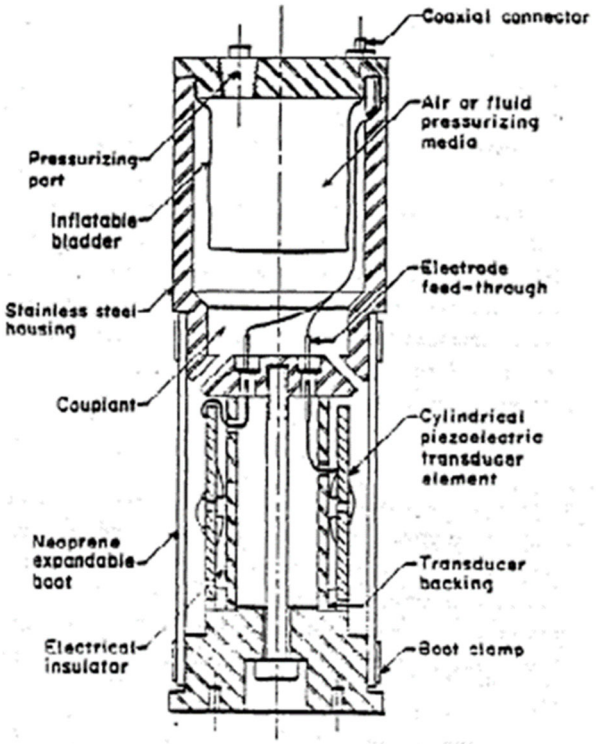

Figure 2-1 Schematic of Thill (1978) Borehole Transducer

Figure 2-2 First Trial of Piezocylinder Source and Power Amplifier

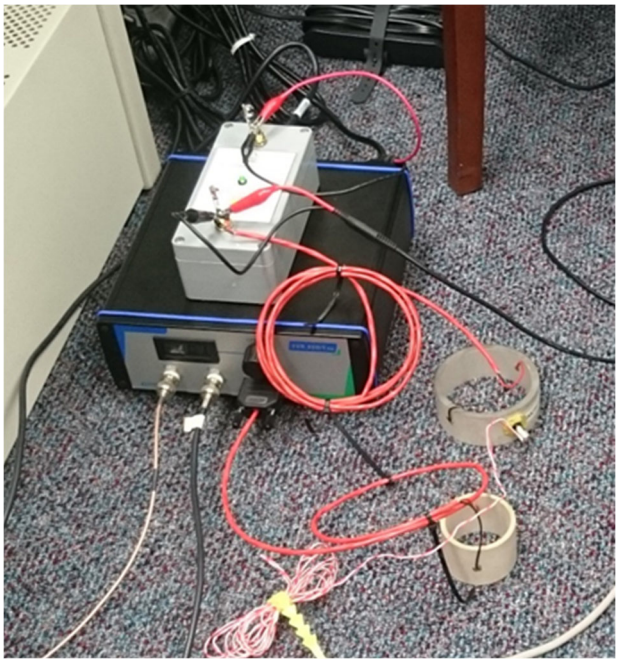

Figure 2-3 Piezoelectric Cylinders and Second Trial of Piezocylinder Amplifier

Figure 2-4 Third Trial of Piezocylinder Borehole Source and Power Amplifier

Figure 2-5 Inflatable Canister for Coupling Piezocylinders with Borehole Wall

However, we discovered from these experiments that the piezoelectric cylinders typically available from manufacturers do not generate the frequency content most desired for our borehole source. The largest cylinder commercially available has a resonant frequency of 14 kHz and a lowest usable frequency for our purposes of about 10 kHz. Our experiments indicate that usable frequencies below 10 kHz will be required to produce a wavefield capable of illuminating a 5-ft radius zone of material around a borehole. The device we constructed works, but the wavefield is primarily of higher frequency and will likely not provide the desired depth of penetration. All of the manufacturers we contacted do not have the capability of constructing a cylinder with a resonant frequency below 14 kHz. As well, if it were possible, such a cylinder would have a diameter larger than 3.5 inch and would likely not fit in a standard 4 inch diameter borehole. This discovery was most unfortunate and unexpected, as we had hoped to utilize the

piezocylinder idea of Thill (1978) for our borehole source and had dedicated a significant amount of time and effort toward this implementation.

2.2.2 Mid-Range Barrel Stave Flextensional Transducer

Based upon a recommendation from a piezoelectric element manufacturer, we found an alternative configuration to the piezocylinders described above for generating monopole wavefields with frequencies below 10 kHz. Figure 2-6 shows a so-called piezoelectric barrel-stave flextensional transducer that is designed for lower frequencies and utilizes a completely different mechanism than the cylinders. The barrel-stave element is driven by a commercially available power amplifier and transformer pair also shown in Figure 2-6. The barrel-stave has been primarily used for underwater sonar applications and thus can be used in a fluid-filled borehole as well as within a fluid-filled inflatable canister like that used to house the piezocylinders. Also similar to the previous piezocylinder-based components described above, the barrel-stave system shown is not immediately available from commercial vendors and must be constructed to order by a manufacturer in Ontario, Canada. The acquisition of the system required a total of eight months to secure all components.

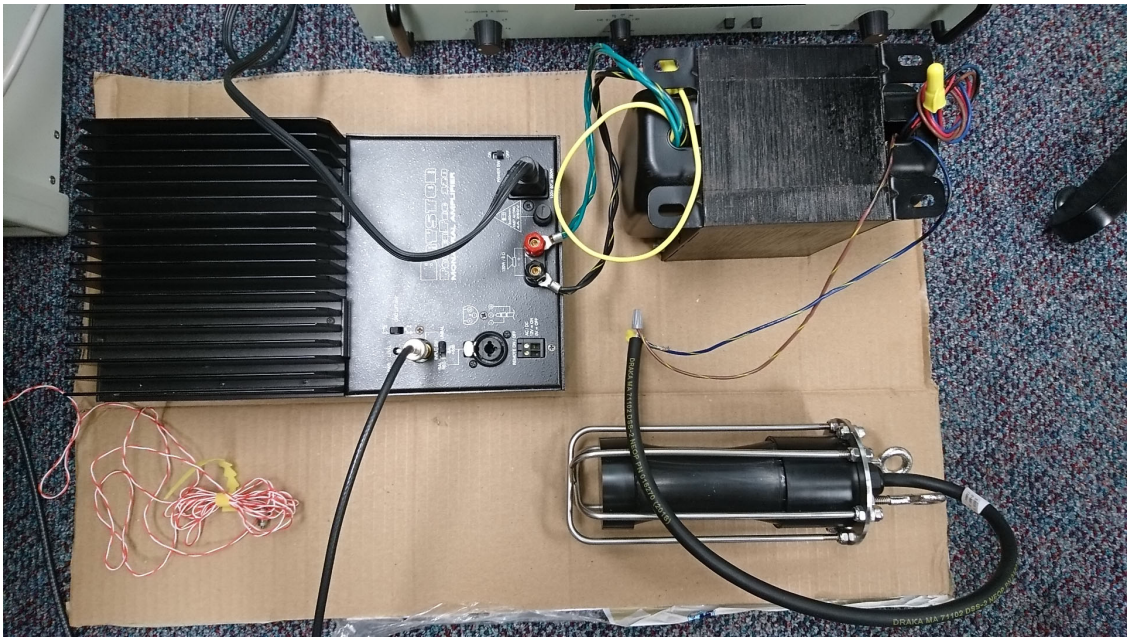

Figure 2-6 Barrel Stave Flextensional Transducer and Power Supplies

2.2.3 Low-Frequency Pneumatic Solenoids

Finally, a third source for generating wavefields from within a borehole is referred to as an SH hammer (Figure 2-7). The hammer was originally designed to produce horizontally polarized shear waves for use in crosshole seismic testing of soils. The source is dipole and not monopole in operation, but it may be possible to utilize this alternative configuration due to the recent development of 3D full waveform models. The horizontal force required to create the SH wave is produced by a series of pneumatically driven solenoids. The SH hammer is connected to a high-pressure air cylinder (Figure 2-8) that provides the supply of air required to fire the solenoids. The high-pressure air cylinder is connected to a double hose reel with both low- and high-pressure lines (Figure 2-9). The high-pressure line supplies air pressure to the hammer so that it can be fired. The low-pressure line is coupled to a triggering mechanism, which allows the hammer to be fired by the operator by merely pushing a button (shown in Figure 2-8 above the tank). The use of the low-pressure line helps to conserve the air supply from the tank and provides a simple manner in which to fire the hammer. Aluminum rods referred to as orientation rods are used to lower the hammer down the hole and to orient the hammer in the proper direction to provide a horizontal traction (Figure 2-10). Another feature of the hammer is that it has an electrical trigger. When the hammer fires, an electrical signal is transmitted to the data acquisition system, providing an exact triggering time that is helpful when averaging consecutive records. The one shortcoming that we have discovered thus far is that the device occupies most of the space within a 4-inch diameter borehole, which has led to difficulty in using it in conjunction with the cabling required for a receiver array in the same borehole.

Figure 2-7 Pneumatic Solenoid SH Source

Figure 2-8 High-Pressure Air Cylinder for Powering Pneumatic Solenoid SH Source

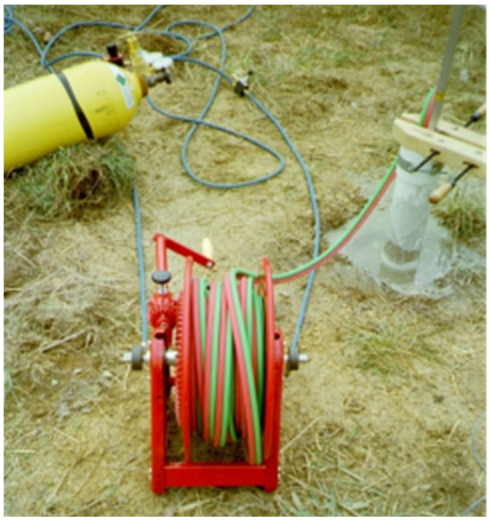

Figure 2-9 Double Hose System for Pneumatic Solenoid SH Source

Figure 2-10 Implementation of Pneumatic Solenoid SH Source in a Borehole

2.3 Receiver

Following the numerical experiments from the previous project, the receiver array was to consist of three-component motion transducers in a single line along the vertical sidewall of a borehole (Figure 2-11). Future work may include simultaneous multiple lines to more efficiently capture a 3D wavefield. Both uniform and non-uniform spacing of the receivers are possible. Some very recent research studies have demonstrated that it may be possible to capture mechanical

wavefield signatures via non-contact sensors that measure the sound of a passing mechanical wave, but it is uncertain whether this technique is possible for the proposed application.

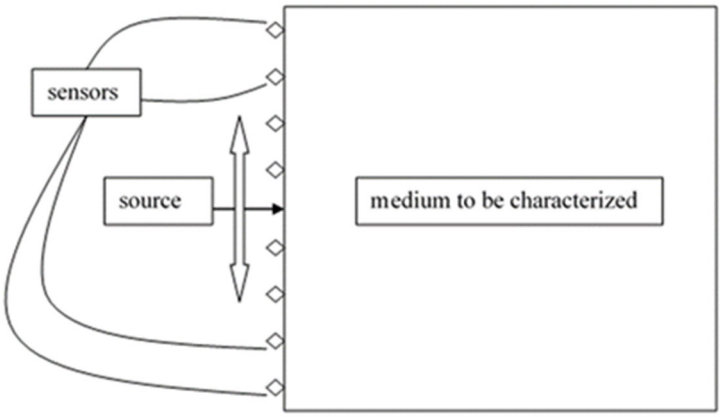

Figure 2-11 Schematic of Borehole Receiver Array

2.3.1 Inflatable Bladder with Accelerometers

We have developed a working inflatable membrane system for a short, high-frequency receiver array that has tested well in the Task 3: Validation Experiments described below (Figure 2-12). Our first experiments have used uniaxial accelerometers for the measurements. We subsequently have purchased and implemented a triaxial accelerometer for use in the final instrument (Figure 2-13). This first design would require revision to work with a longer array of 10 to 12 three-component accelerometers in a line along the vertical sidewall of a borehole.

Figure 2-12 Kalinski-Type Bladder Shown Inflated Inside an Acrylic Tube

Figure 2-13 Three-Component Accelerometer

To couple the receiver array to a borehole wall, a Kalinski-style membrane system is utilized. (Kalinski 2012). This idea was developed for crosshole and down-hole test sensors by Michael Kalinski at the University of Kentucky. Here, the receivers are attached (glued) to the inside of a cylindrical membrane constrained on each end via metal end caps (like a triaxial test specimen).

The membrane is then inflated within the borehole to couple the sensor with the borehole wall. A stud and washer system (Figure 2-14) is utilized to provide direct contact between the accelerometer and borehole wall while still maintaining a leak-proof membrane. This design was found a necessary modification to capture high-frequency waveforms that are otherwise dampened by the membrane if the accelerometer is glued to inside of membrane but without a pass-through stud.

Figure 2-14 Stud and Washer System for Contacting Accelerometer to Borehole Wall

2.3.2 3D Geophone String

As a second receiver array option, we also have a borehole string of 3D geophones that can be used for the field experiments. The string consists of eight, three-component geophone pods spaced at 1-m intervals (Figure 2-15). The string is coupled to the inside of a borehole wall via an inflatable fire hose that is connected to the high-pressure air cylinder previously shown in Figure 2-8.

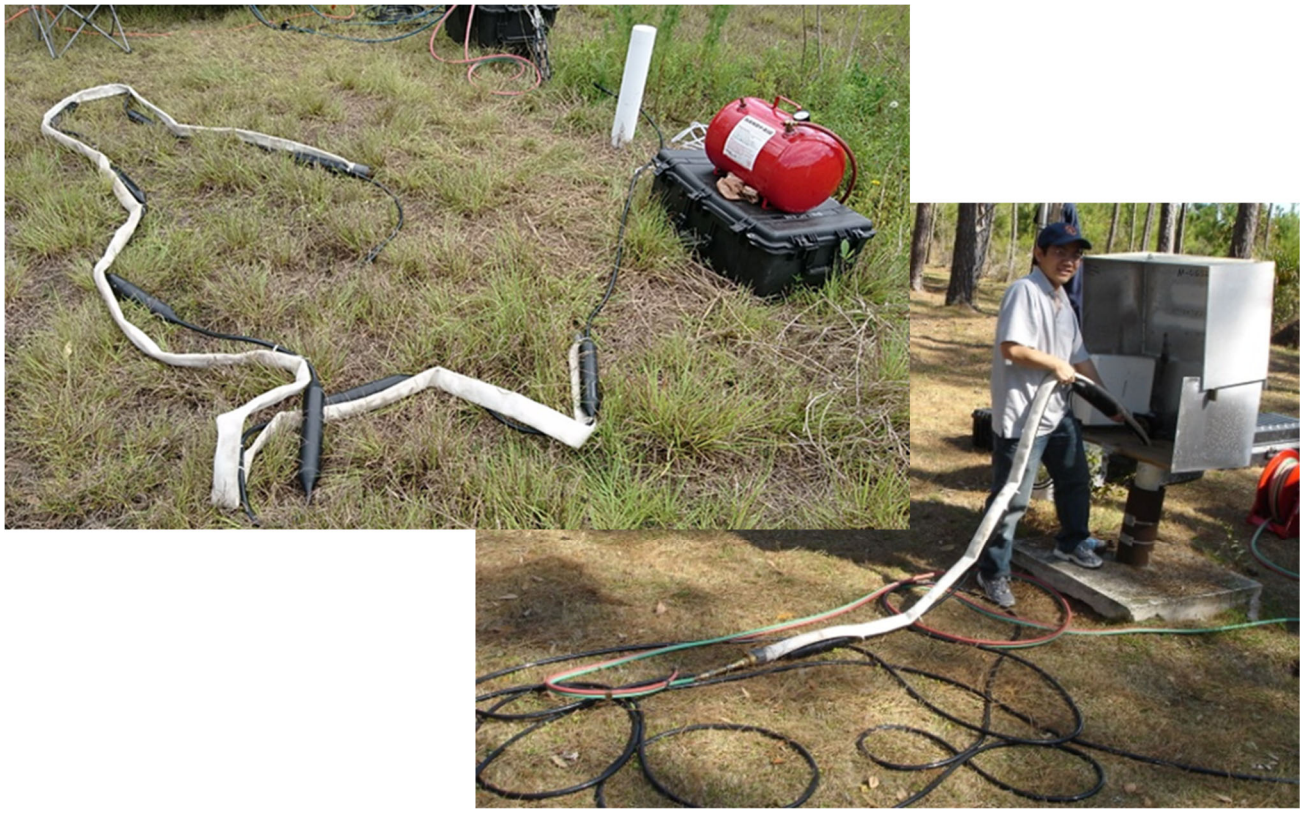

Figure 2-15 3D Geophone Borehole String

CHAPTER 3
TASK 2: INVERSION SOFTWARE

3.1 Introduction

In this part of the study, an analysis software was developed to create an image of the material adjacent to the borehole based on the full wave inversion (FWI) technology. In order to perform FWI within a borehole, the cylindrical geometry and the associated boundary conditions must be modeled correctly. Due to the formidable computer time of 3D borehole inversion, an ABAQUS-based axisymmetric forward model was chosen for the proposed imaging effort. The inversion was based on a regularized Gauss-Newton method implemented in MATLAB. The interface between ABAQUS and MATLAB was developed using Python script. This document begins with a brief description of practical strategies employed in the FWI to ensure convergence, followed by a detailed illustration of the implementation of these strategies in the software and the effectiveness of the software through three example simulation cases. Finally, guidelines in terms of installation and recommended procedure to run the software are provided for users.

3.2 Practical Strategies for FWI

Inverse problems are generally very difficult. The difficulties stem from three issues: existence, uniqueness, and instability (Aster et al., 2005). First, inverse problems may not have a solution due to inexact physics in the forward model or noise in the data. Second, there may be an infinite number of models that can fit the data equally well. Lastly, inverse problems may be ill-posed or ill-conditioned, where the solution is very sensitive to small changes in the data. For problems with solutions always exist, the issues of uniqueness and instability can be largely solved using regularization. Nonetheless, another important issue exists: convergence. Depending on the initial model, local optimization techniques (e.g., regularized Gauss-Newton method) may converge to a local minimum. As a result, two strategies: (i) frequency filtering; and (ii) temporal windowing are implemented in the inversion software to help find the global minimum as described below.

3.2.1 Frequency filtering

To mitigate nonlinearity and loosen the initial model requirement, a multiscale approach is often utilized in either time domain (Bunks et al., 1995) or frequency domain (Sirgue and Pratt, 2004). This multiscale approach builds a background model by inverting the low-frequency component, and then increases the resolution by gradually adding high-frequency components in the data. The degree of nonlinearity, or the multimodal distribution of the misfit function with respect to the model parameters, depends on the frequency content of seismic data. The misfit (objective) function is more linear at low frequencies than at high frequencies. For this reason, inversion processes that sequentially proceed from low to high frequencies are more likely to reach the global minimum than processes that start with high-frequency raw data.

For example, Figure 3-1 displays the time signal and the associated frequency content of the raw data in the top and bottom subparts, respectively. It is important to note that the frequency spectrum in the raw data is being dominated by three peaks, approximately centered at 500, 1500, and 2500 Hz. After applying a low-pass filter (500-1000 Hz), only the lowest peak remains in the spectrum and the time signal becomes more linear and smoother, as shown in Figure 3-2. An inversion process that begins with the filtered data in Figure 3-2 (with only low-frequency components) is more likely to find the global minimum than a process that proceeds directly with the raw data in Figure 3-1.

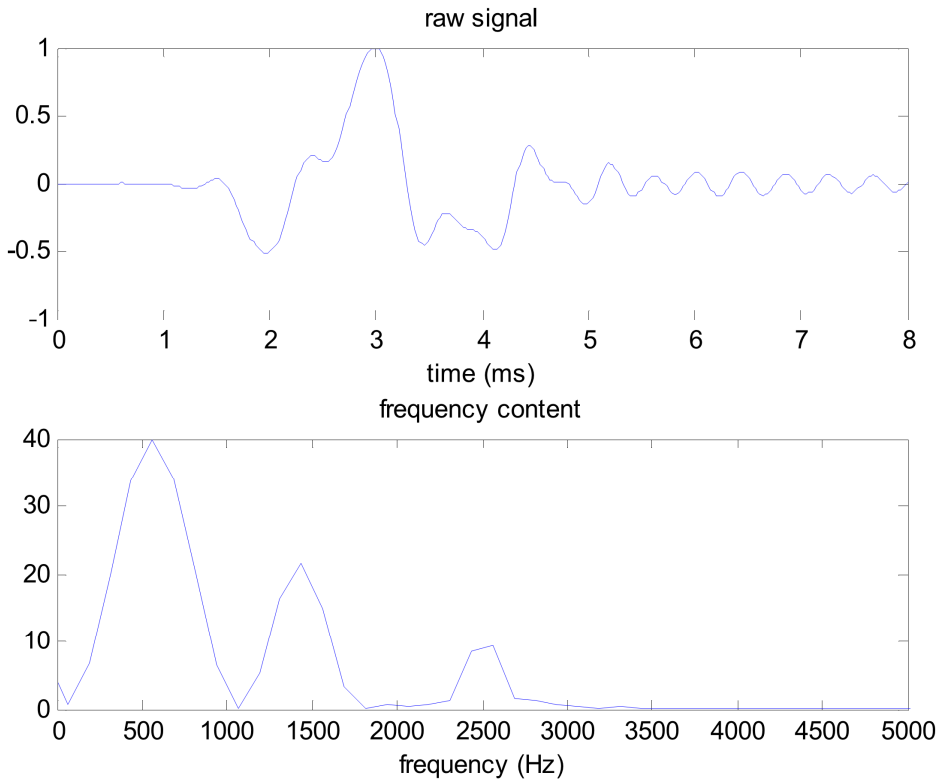

Figure 3-1 Time signal and frequency spectrum of raw data

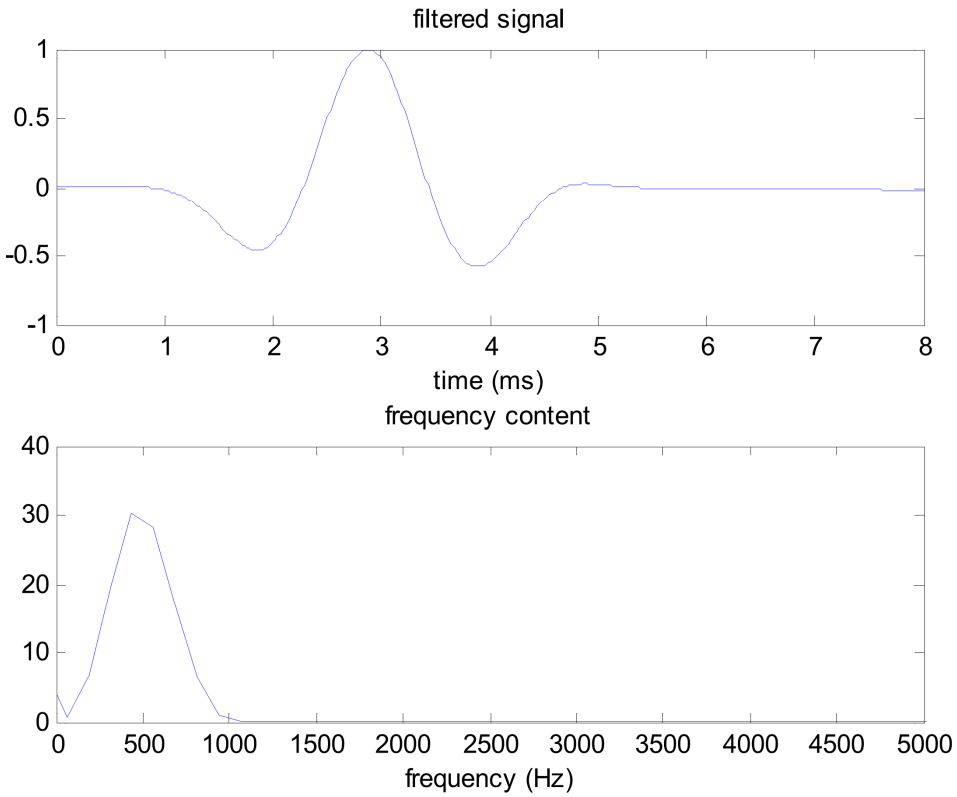

Figure 3-2 Time signal and frequency spectrum after frequency-filtering

3.2.2 Temporal windowing

To further reduce the nonlinearity, this study proposes starting with a short time window at a low-frequency band, and then gradually increasing the time window and frequency bandwidth. Figure 3-3 illustrates the combined frequency-filtering and temporal-windowing technique. For the filtered waveform shown in Figure 3-2, the first window was clipped at 2.5 ms, and the second window was clipped at 5 ms, with the full window corresponding to the entire length of the signal. For the first time window, inversion was started using the filtered data (i.e., at a low-frequency band). After convergence is reached based on predefined criteria, further inversion was conducted for the same time window using the raw data. Then, the inversion was continued with longer time windows, followed by similar filtering strategies, until the full data set has been considered.

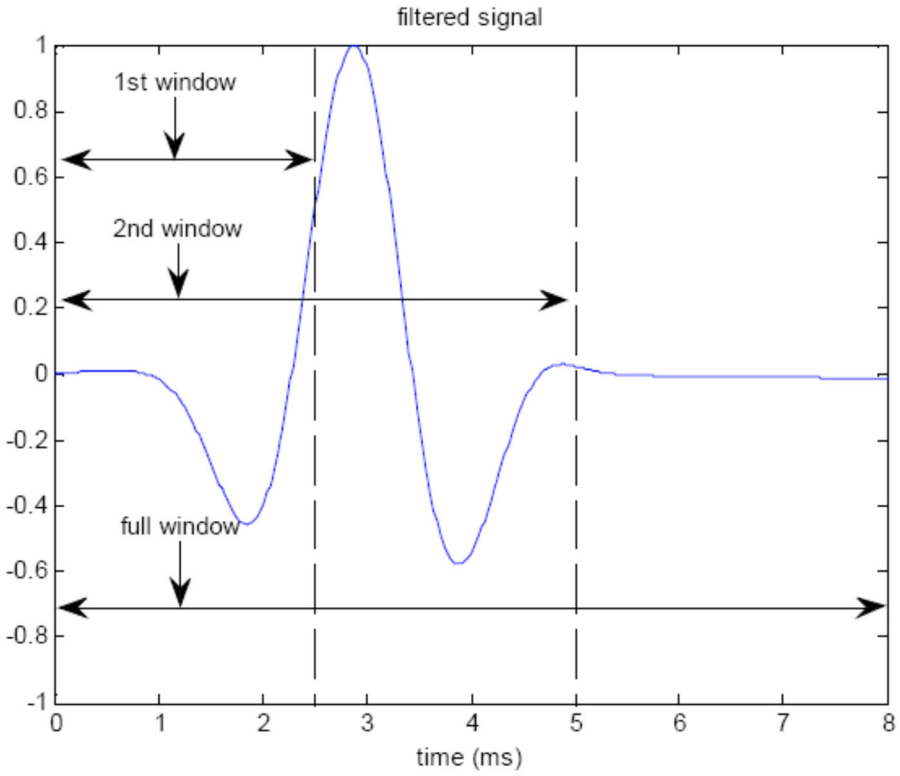

Figure 3-3 Temporal windowing: gradually increasing the time to facilitate convergence

3.3 Example Simulations

The inversion software developed and compiled using MATLAB R2013b as part of the study is termed as FWIRA, denoting a **f**ull **w**ave **i**nversion technology based on **r**egularized Gauss-Newton method using **a**xisymmetric forward model. This section provides three example simulations to illustrate the effectiveness of the inversion software FWIRA for multilayered systems without anomaly, with one ring-type anomaly, and with two ring-type anomalies, respectively. The synthetic records for each example were generated using an axisymmetric forward model (Figure 3-4) and treated as field data. The velocity profile was then reconstructed by means of inversion. Theoretically, all inverted profiles should be the same as the assumed known models used to create the synthetic records.

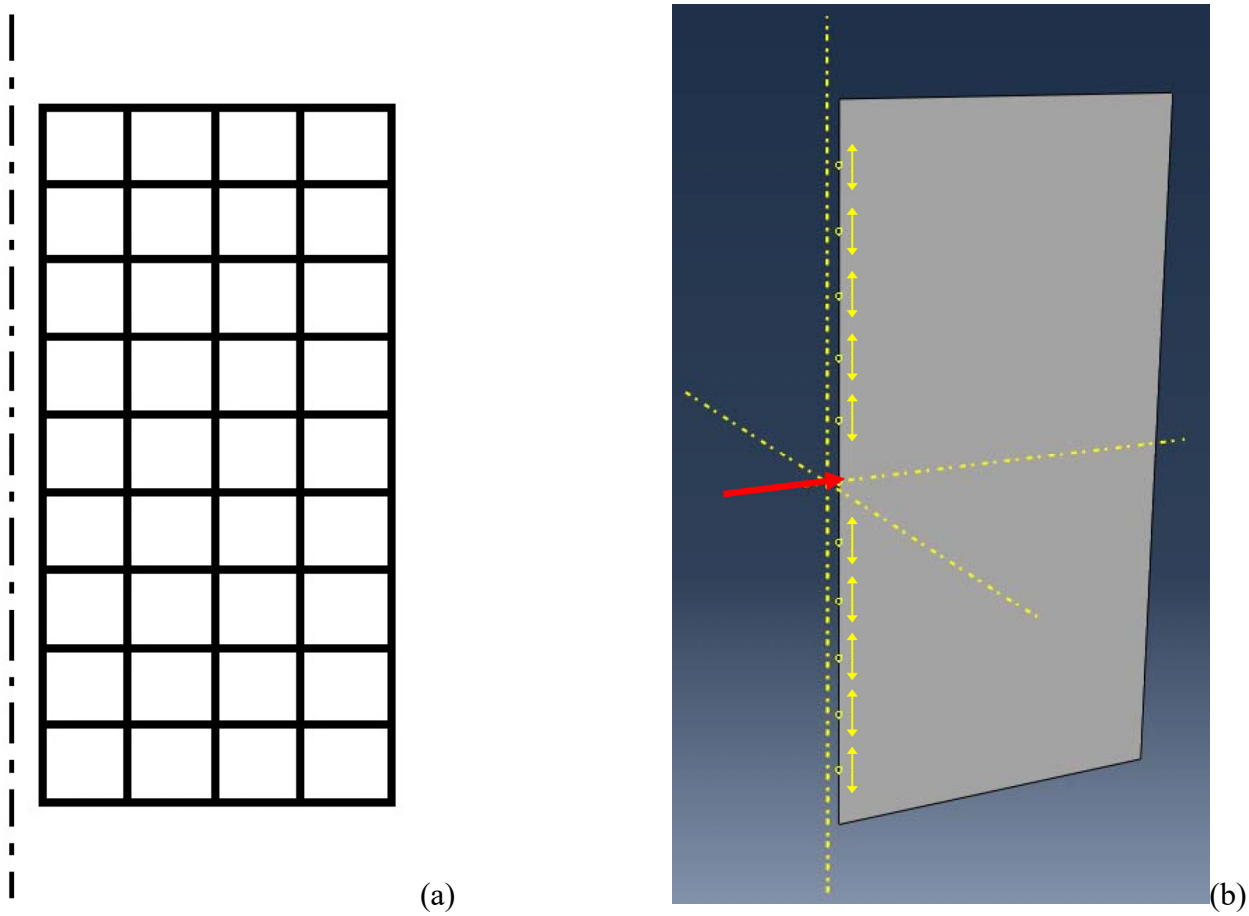

(a) (b)

Figure 3-4 Axisymmetric forward model: (a) borehole model discretization; (b) schematic loading and layout of signal receivers

As shown in Figure 3-4(a), the axisymmetric forward model representing a cylindrical body of soil surrounding a borehole of 0.2 m in diameter, was uniformly discretized into 36 pixels (9 by 4), and shear wave velocity values were assigned independently to each pixel (0.5 m by 0.5 m), resulting in 36 model parameters. Figure 3-4(b) shows a shock loading excited at the center of the side wall of the borehole, and a 10-channel receiver array uniformly placed along the wall, with the nearest offset and trace interval being 0.5 m. Figure 3-5(a) presents the shock loading, and Figures 3-5(b) to 3-5(d) show the 4 ms of synthetic records (i.e., the axial component of the particle displacements) obtained for the three aforementioned multilayered systems, respectively. Inversions were carried out by matching the axial component of the particle displacements.

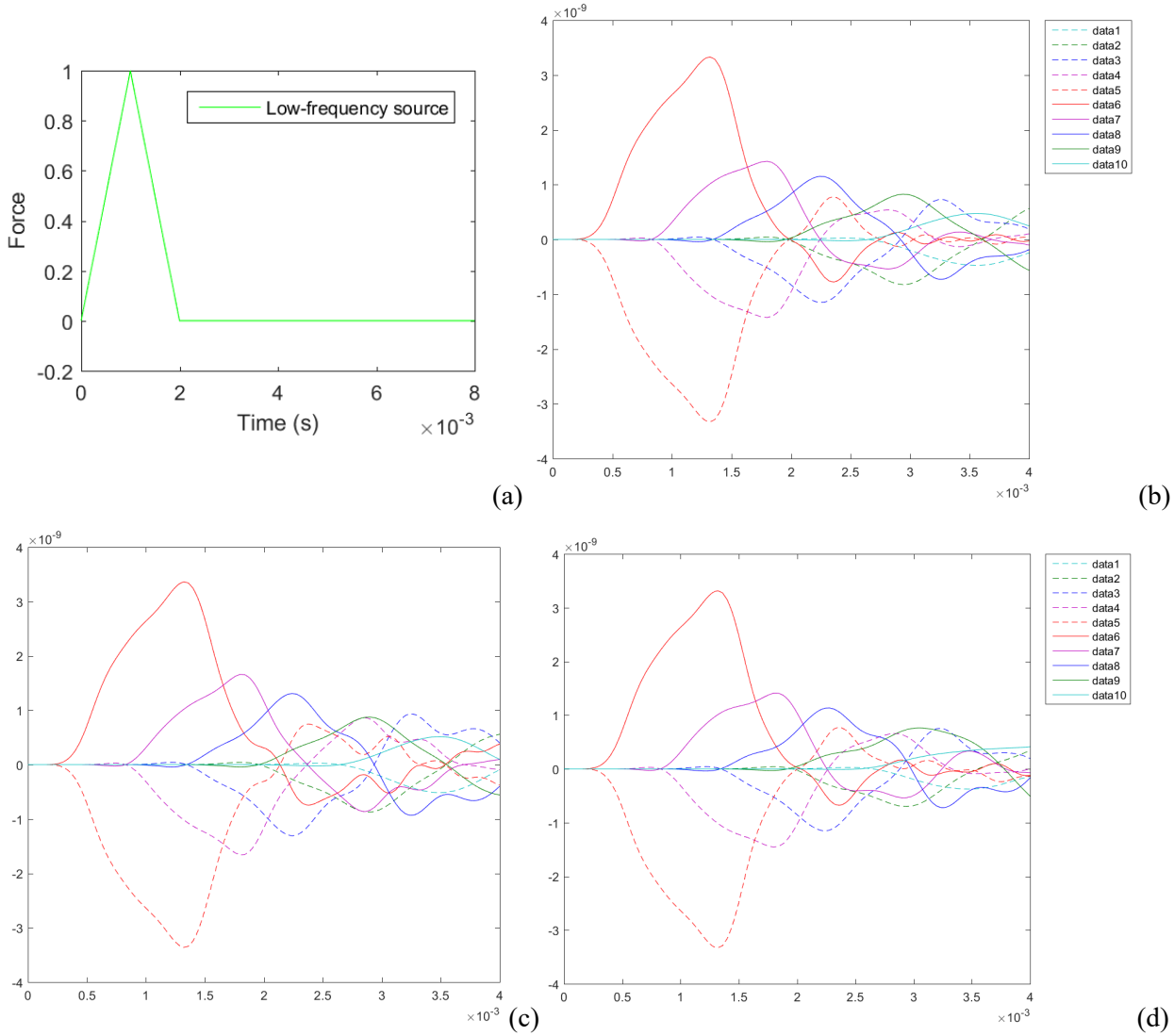

Figure 3-5 (a) A triangular wavelet source; and synthetic axial displacements for (b) multilayered system w/o anomaly; (c) multilayered system with one anomaly; (d) multilayered system with two anomalies

It is important to note that in the current implementation, only the shear wave velocity was inverted, while the Poisson's ratio (0.25) and mass density (2,000 kg/m^3) remained constant during the inversion. The amplitude of the displacements and the L2 norm of the misfit function were normalized for ease of comparison.

Following the practical strategies described in Section 3.2, the inversion was divided into four steps: (i) a short time window of 2 ms when a low-pass filter was applied to the associated waveforms; (ii) the same 2-ms time window with no filter applied; (iii) a full time window of 4 ms with a low-pass filter applied; and (iv) the same 4-ms time window with no filter applied. The shear wave velocity of the initial model was set to be 775 m/s uniformly across all pixels for the first step, and then the updated model at the end of each step was used as the initial model for the immediate next step. Generally, a least square error (LSE) of no greater than 1 micron will lead to well-converged results (i.e., well-matched waveforms) for each step. In the example simulations, 0.1, 0.5, 0.75, and 0.75 microns were used as the LSE criteria for steps 1 through 4, respectively (Table 3-1). The maximum number of iterations (k_{max}) was set to be 50, 75, 75, and 100 for each corresponding step to confine program running time within a reasonable range. For a standard personal computer, the running time for one complete simulation typically does not exceed 12 hours.

Table 3-1 Summary of stepwise convergence criteria and resulting LSE and k for each case

Case No.	Step 1	Step 2	Step 3	Step 4	Step 1	Step 2	Step 3	Step 4	**Σk**
	(LSE Criterion)				(k_{max})				
	(1.0E-7)	(5.0E-7)	(7.5E-7)	(7.5E-7)	(50)	(75)	(75)	(100)	
	LSE				**k**				
1	9.8E-8	4.8E-7	9.4E-7	3.8E-6	13	16	75	100	204
2	9.5E-8	4.9E-7	7.4E-7	7.3E-7	20	38	49	12	119
3	3.3E-7	5.8E-6	7.4E-7	7.3E-7	50	75	40	53	218

Note: LSE denotes least square error, k is # of iterations and k_{max} is the maximum allowed # of iterations.

3.3.1 Case 1: Multilayered soil profile without anomaly

The model in Case 1 is comprised of nine distinct velocity layers, each 0.5 m thick. The shear wave velocity varied gradually from 450 m/s at the top, to 1000 m/s in the middle, and back to 450 m/s at the bottom. This model was chosen because a majority of geological materials are multilayered.

As shown in Table 3-1, the LSE criteria were met after only 13 and 16 iterations for Steps 1 and 2 respectively, indicating the inversion converged very rapidly for the first two steps. The LSE criterion was not met for Step 3, and inversion was terminated after 75 iterations (the specified maximum number). However, it can be seen that at the end of Step 3 the layered structure became identifiable (Figure 3-6(a)) and the waveforms matched well across all channels (Figure 3-6(b)). A close look at the L2 norm convergence curve (Figure 3-6(c)) revealed that the convergence rate was high for the first five iterations, and then it reduced significantly and became almost zero after twenty iterations. So, the solution illustrated in Figure 3-6(a) was considered to be a good initial model for further velocity updates. Similarly, the LSE criterion was not met for Step 4, and inversion was terminated after the specified maximum number of iterations. Nevertheless, Figures 3-7(a) and 3-7(b) show that the layered structure of the final inverted model was very well recovered and the waveforms were in very good agreement across all channels. Only some smearing is visible in the last column where the model parameters were less constrained by the acquired data. Figure 3-7(c) shows that the convergence rate reduced to almost zero after sixty iterations, despite the step exhibited a slower overall convergence rate than that of the prior step.

3.3.2 Case 2: Multilayered soil profile with one ring-type anomaly

The model in Case 2 is similar to the one in Case 1, except that a ring-type (0.5 m wide), low-velocity (V_s = 450 m/s) anomaly was introduced 1.0 m away from the wall in the middle layer. As shown in Table 3-1, the LSE criteria were met after 20, 38, 49 and 12 iterations respectively for Steps 1 through 4. Figure 3-8(a) illustrates that both the layered structure and the anomaly were successfully recovered at the end of Step 4. The inverted shear wave velocity value was 447 m/s for the anomaly. Some smearing is visible in the last column where the model

parameters were less constrained by the acquired data. The wave forms were well matched (Figure 3-8(b)), and the convergence rate was fast (Figure 3-8(c)).

3.3.3 Case 3: Multilayered soil profile with two ring-type anomalies

The model in Case 3 also has a layered structure similar to Cases 1 and 2, but it includes two ring-type (both 0.5 m wide), low-velocity (V_s = 450 m/s) anomalies: one is located 1.0 m away from the wall in the third layer and the other is 0.5 m away from the wall sitting in the seventh layer.

As shown in Table 3-1, the LSE criterion was not met for Step 1, and inversion was terminated after 50 iterations (the specified maximum number). However, it can be seen that at the end of Step 1 the layered structure in the first column was well recovered and the anomaly in the second column became identifiable (Figure 3-9(a)). Furthermore, the waveforms matched well across all channels (Figure 3-9(b)), and the convergence rate became almost zero after ten iterations (Figure 3-9(c)). So, the solution illustrated in Figure 3-9(a) was considered to be a good initial model for further velocity updates. Similarly, the LSE criterion was not met for Step 2, and inversion was terminated after 75 iterations (the specified maximum number). Nevertheless, it can be seen that at the end of Step 2 the anomaly in the second column was well recovered and the layered structure in the first two columns became identifiable (Figure 3-10(a)). Furthermore, the waveforms matched well across all channels (Figure 3-10(b)), and the convergence rate became almost zero after twenty iterations (Figure 3-10(c)). So, the solution illustrated in Figure 3-10(a) was considered to be a good initial model for the following step. The LSE criteria were met after 40 and 53 iterations for Steps 3 and 4 respectively, indicating well converged results for the last two steps. Figure 3-11(a) illustrates that both the layered structure and the two anomalies were successfully recovered at the end of Step 4. The inverted shear wave velocity value was 447 m/s for the anomaly in Layer 3 and 448 m/s for the one in Layer 7. The wave forms were well matched (Figure 3-11(b)), and the convergence rate became almost zero after forty iterations (Figure 3-11(c)). Table 1-1 summarizes the total number of iterations conducted to recover model parameters for all three cases. As expected, Case 2 where the LSE criteria were met for all steps, required the least number of iterations for a converged solution.

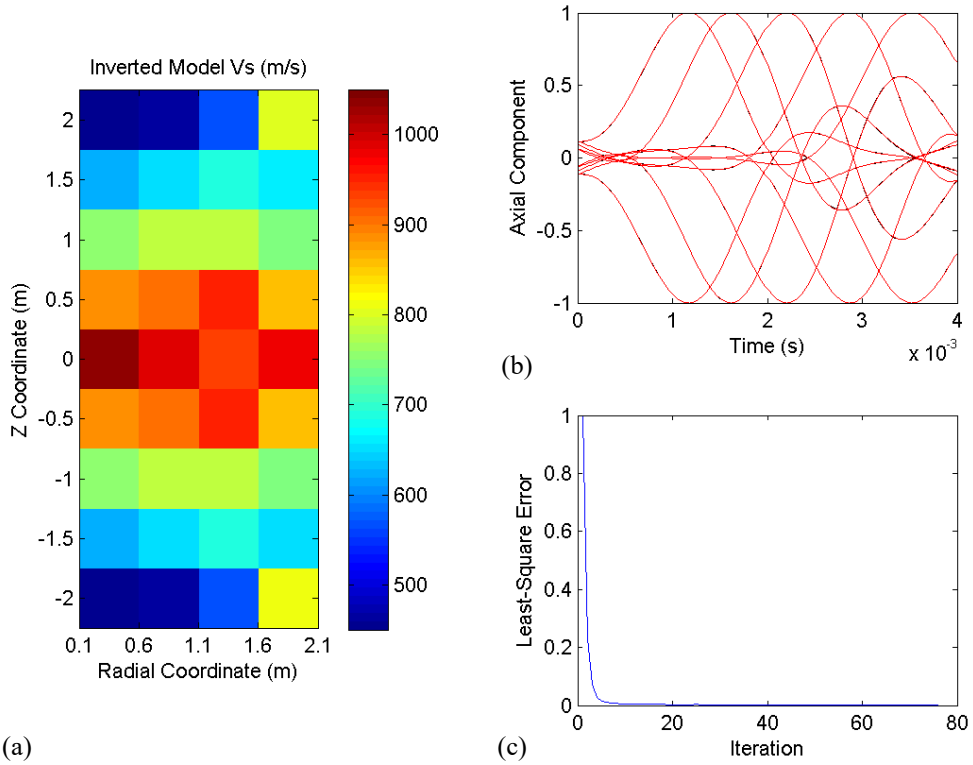

Figure 3-6 Results of Step 3 for Case 1: multilayered system without anomaly

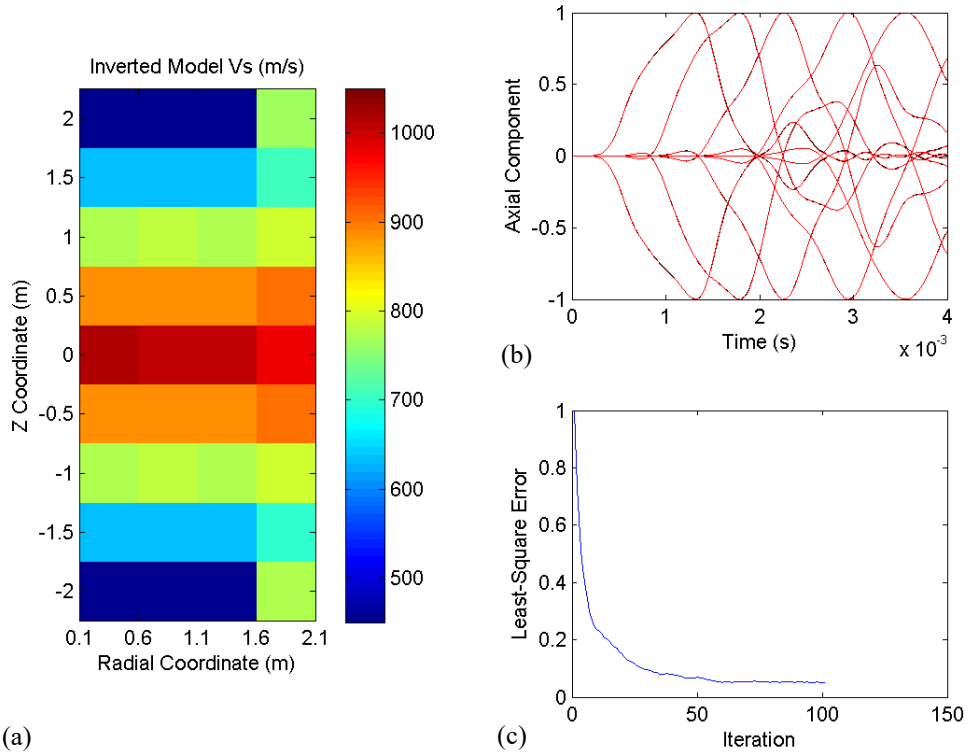

Figure 3-7 Results of Step 4 for Case 1: multilayered system without anomaly

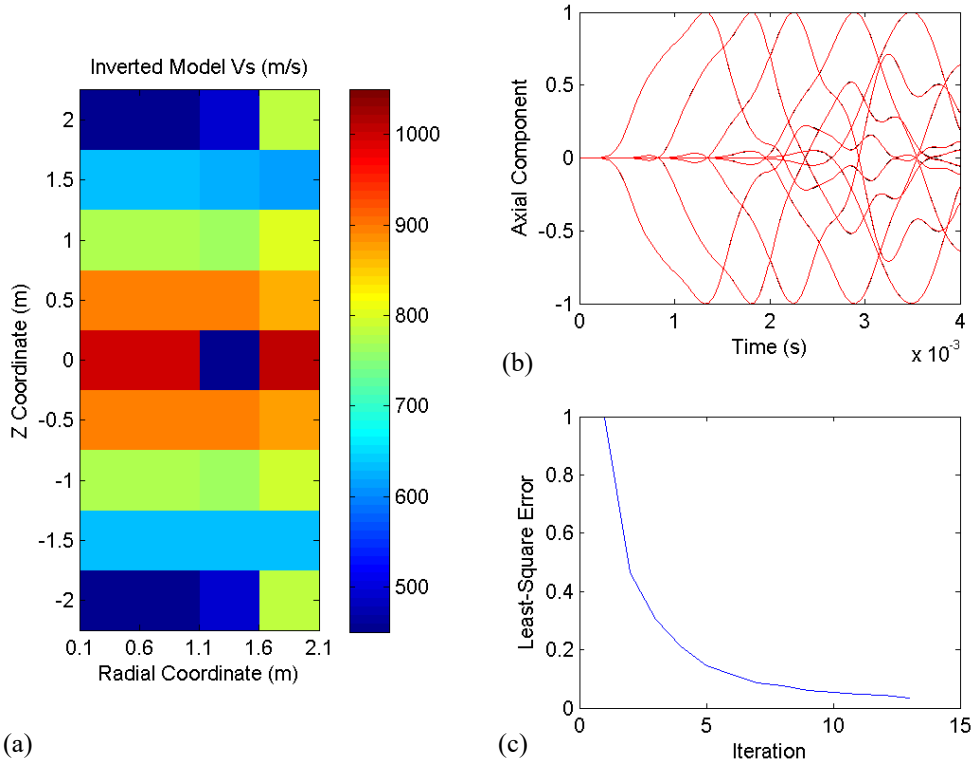

Figure 3-8 Results of Step 4 for Case 2: multilayered system with one ring-type anomaly

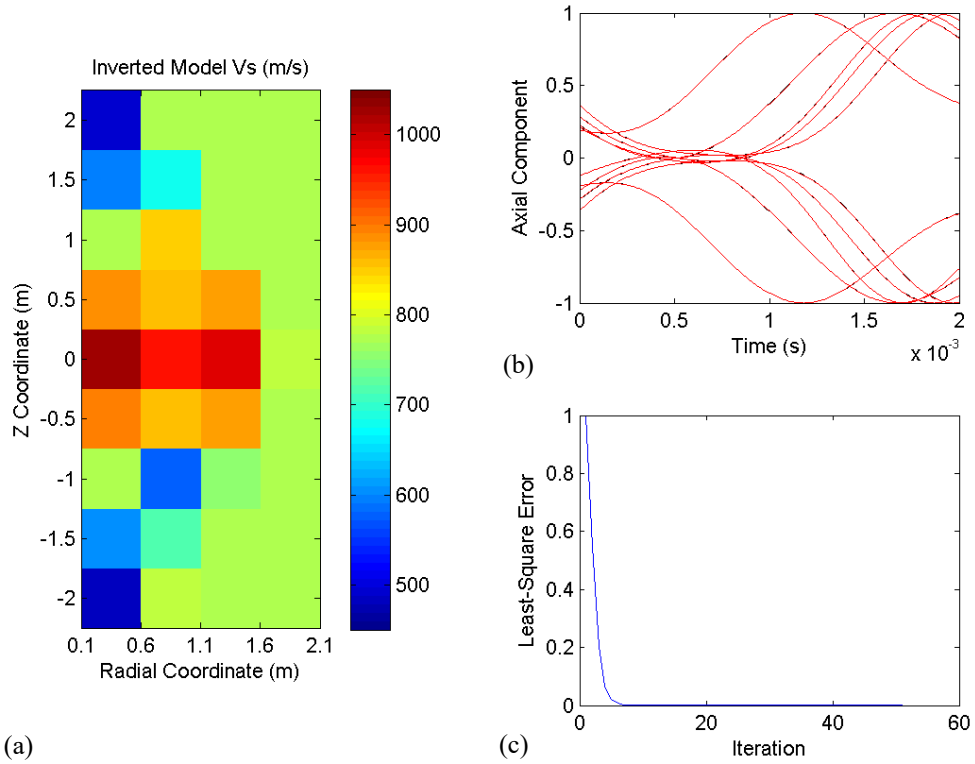

Figure 3-9 Results of Step 1 for Case 3: multilayered system with two ring-type anomalies

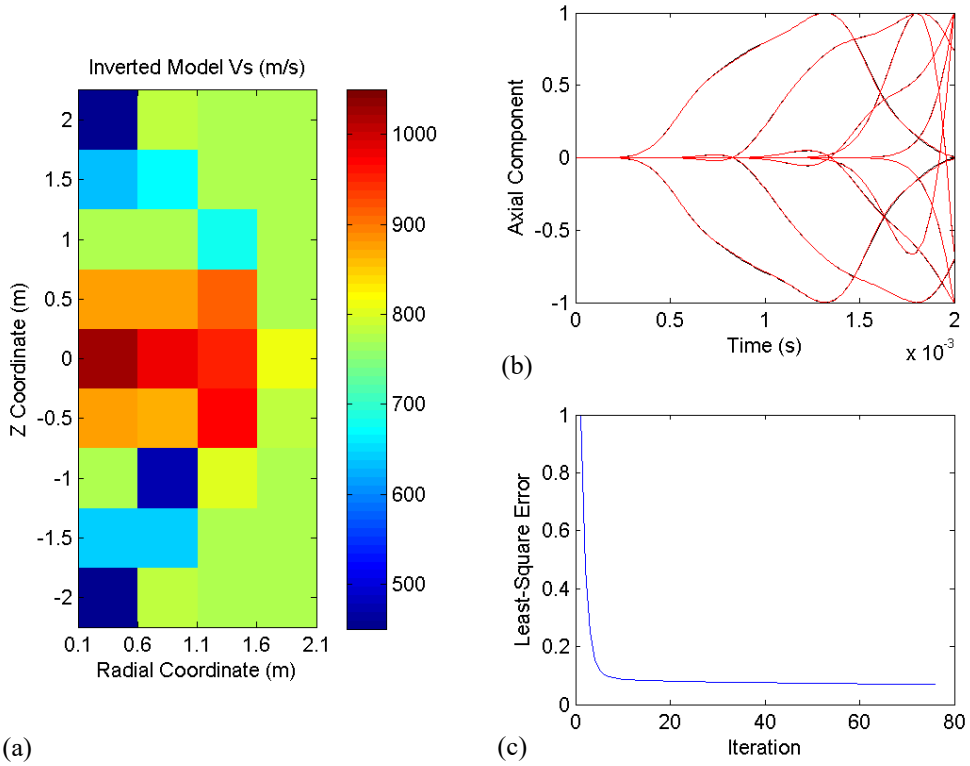

Figure 3-10 Results of Step 2 for Case 3: multilayered system with two ring-type anomalies

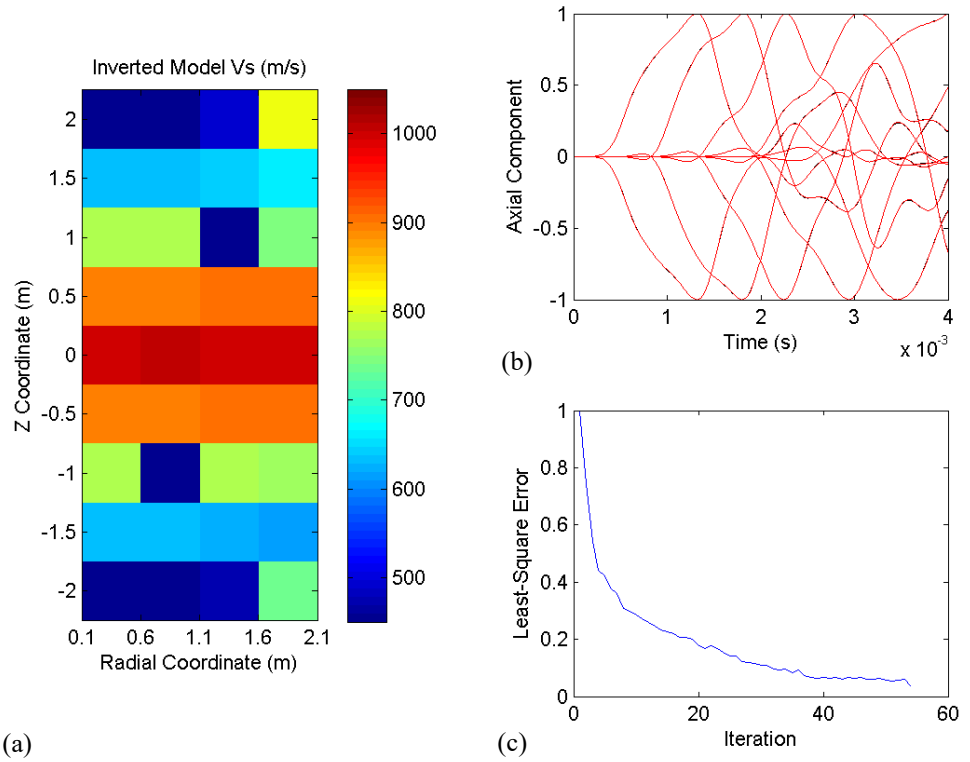

Figure 3-11 Results of Step 4 for Case 3: multilayered system with two ring-type anomalies

3.4 Guidelines for Users of FWIRA

As described earlier, the full wave inversion was conducted following a four-step approach designed based on the joint use of temporal-windowing and frequency-filtering techniques to help converge to the global minimum more effectively. Therefore, four executive files were included in the inversion software FWIRA, i.e., *_s1, *_s2, *_s3 and *_s4 (* denotes Borehole_readingXSE). Each file represents one step and is implemented consecutively to complete the inversion procedure. An initial model is required for starting the inversion for each of the steps. The initial model for Step one need to be determined based on existing soil information surrounding the borehole, while the initial model for any successive step is simply obtained from the updated model at the end of the prior step.

3.4.1 Installation

The inversion software FWIRA has been compressed into one file, i.e., 'FWIRA.zip'. It can be installed by copying the zip-file to the target computer and extracting the files to the selected destination (e.g., My Computer\Documents\MATLAB). Once the procedure is completed, a folder named demo-exe should appear under the installation directory which includes:

- Four executive files: *_s1, *_s2, *_s3 and *_s4 (* denotes Borehole_readingXSE)
- Three sub-folders; each includes one example simulation
    - Case1-HLayer-NoAnomaly
    - Case2-HLayer-OneAnomaly
    - Case3-HLayer-TwoAnomalies
- Two inp-files; each includes one axisymmetric forward model
    - A1.inp (used to predict displacements for the short-time window)
    - A.inp (used to predict displacements for the full-time window)
- One py-file (python script)
    - B.py (used to acquire displacements at locations of a 10-channel receiver array)

In addition, the MATLAB Complier Runtime (MCR) V8.2 and the ABAQUS Student Edition V6.11SE are required to be installed in the target computer following the setup wizard integrated

as part of the two programs. Both programs are provided along with the FWIRA zip-file to form a complete simulation package as listed below. It is important to note that upon completion of installation of all programs, the target computer need to be rebooted before launching the FWIRA executive files.

- FWIRA.zip
- MCR_R2013b_win64_installer.exe
- Abaqus611SE_win86_64.exe

3.4.2 Tutorial to Run the Examples

The FWIRA program is bundled with three example cases that help explain the inversion simulation. A detailed description of the three example cases and the corresponding simulation results has been provided in Section 3.3. The example files are located in the "<installation directory\demo-exe>" folder. Each example file includes two sub-folders as shown below:

- required_files
    - data_syn_short.txt
    - data_syn_medium.txt
    - PgmInput.xlsx (with four Excel Sheets/Tabs)
        - stage1i; stage2i; stage3i; and stage4i
    - PgmOutput.xlsx (with four Excel Sheets/Tabs)
        - stage1o; stage2o; stage3o; and stage4o
- inversion_results
    - PgmInput_f.xlsx
    - PgmOutput_f.xlsx
    - Four tiff-image files: vs-s1; vs-s2; vs-s3; and vs-s4

The 'required_files' sub-folder includes four files. "data_syn_short" and "data_syn_medium" are synthetic records treated as field measurements, which were generated using an axisymmetric forward model for a short time window and a full time window, respectively. "PgmInput" has four excel sheets/tabs, each contains input information required for launching inversion for the corresponding step. As an example, Figure 3-12(a) shows the input information required for Step 1, including the elastic modulus (in Pa) of the initial model across all pixels, the LSE criterion,

and the maximum allowed number of iterations. Similarly, “PgmOutput” has four excel sheets/tabs, each contains output information at the end the corresponding step. Figure 3-12(b) shows the output information requested for Step 1, including the elastic modulus (in Pa) of the updated model, the LSE value, the actual number of iterations and the computer running time. The ‘inversion_results’ sub-folder provides the users a complete set of inversion results of the simulation case for reference purpose, including two excel files and four tiff-image files.

The following steps need to be taken to perform a simulation using any of the example cases:

- Copy all four files in the ‘required_files’ sub-folder and paste them to the working directory “<installation directory\demo-exe>”.
- Open “PgmInput” in MS Excel and make sure all input information in Sheet/Tab “stage1i” is correct, including elastic moduli of the initial model, the LSE criterion, and the maximum allowed number of iterations.
- Double click the inversion executive file for Step 1, i.e., “Borehole_readingXSE_s1”; The program will launch a dos command window that shows the status of the run (in about ten seconds).
- Close the plot of inversion results once the run is completed for Step 1; The command window will exit automatically; Note that the output information has been saved in Sheet/Tab “stage1o” of “PgmOutput”.
- Open “PgmOutput” in MS Excel; copy elastic moduli of the updated model in Sheet/Tab “stage1o” (i.e., the resulting model of Step 1) and paste them to the reserved places for elastic moduli of the initial model in Sheet/Tab “stage2i” of “PgmInput” (i.e., the initial model of Step 2).
- Close “PgmOutput” and make sure all input information in Sheet/Tab “stage2i” of “PgmInput” is correct.
- Start the inversion simulation for Step 2 by double clicking the inversion executive file “Borehole_readingXSE_s2”.
- Repeat the same operations until completion of simulation for Step 4.

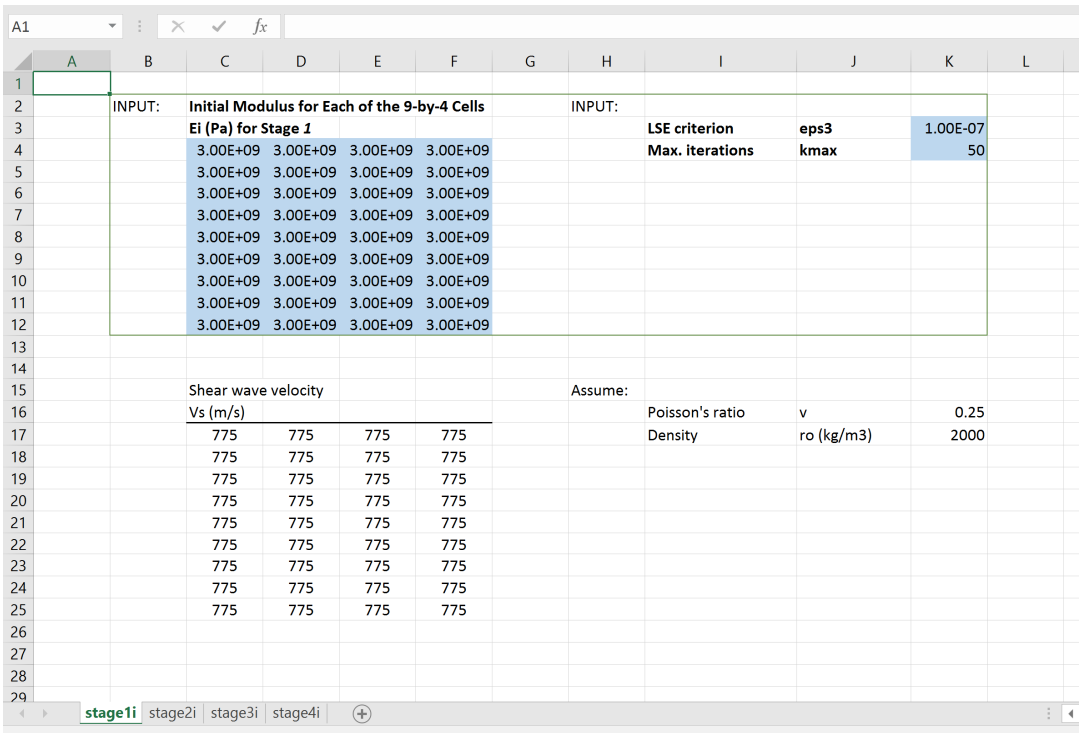

1											
2	INPUT:	**Initial Modulus for Each of the 9-by-4 Cells**					INPUT:				
3		**Ei (Pa) for Stage *1***						**LSE criterion**	**eps3**	1.00E-07	
4		3.00E+09	3.00E+09	3.00E+09	3.00E+09			**Max. iterations**	**kmax**	50	
5		3.00E+09	3.00E+09	3.00E+09	3.00E+09						
6		3.00E+09	3.00E+09	3.00E+09	3.00E+09						
7		3.00E+09	3.00E+09	3.00E+09	3.00E+09						
8		3.00E+09	3.00E+09	3.00E+09	3.00E+09						
9		3.00E+09	3.00E+09	3.00E+09	3.00E+09						
10		3.00E+09	3.00E+09	3.00E+09	3.00E+09						
11		3.00E+09	3.00E+09	3.00E+09	3.00E+09						
12		3.00E+09	3.00E+09	3.00E+09	3.00E+09						
13											
14											
15		Shear wave velocity					Assume:				
16		Vs (m/s)						Poisson's ratio	v	0.25	
17		775	775	775	775			Density	ro (kg/m3)	2000	
18		775	775	775	775						
19		775	775	775	775						
20		775	775	775	775						
21		775	775	775	775						
22		775	775	775	775						
23		775	775	775	775						
24		775	775	775	775						
25		775	775	775	775						
26											
27											
28											
29											

stage1i | stage2i | stage3i | stage4i

(a)

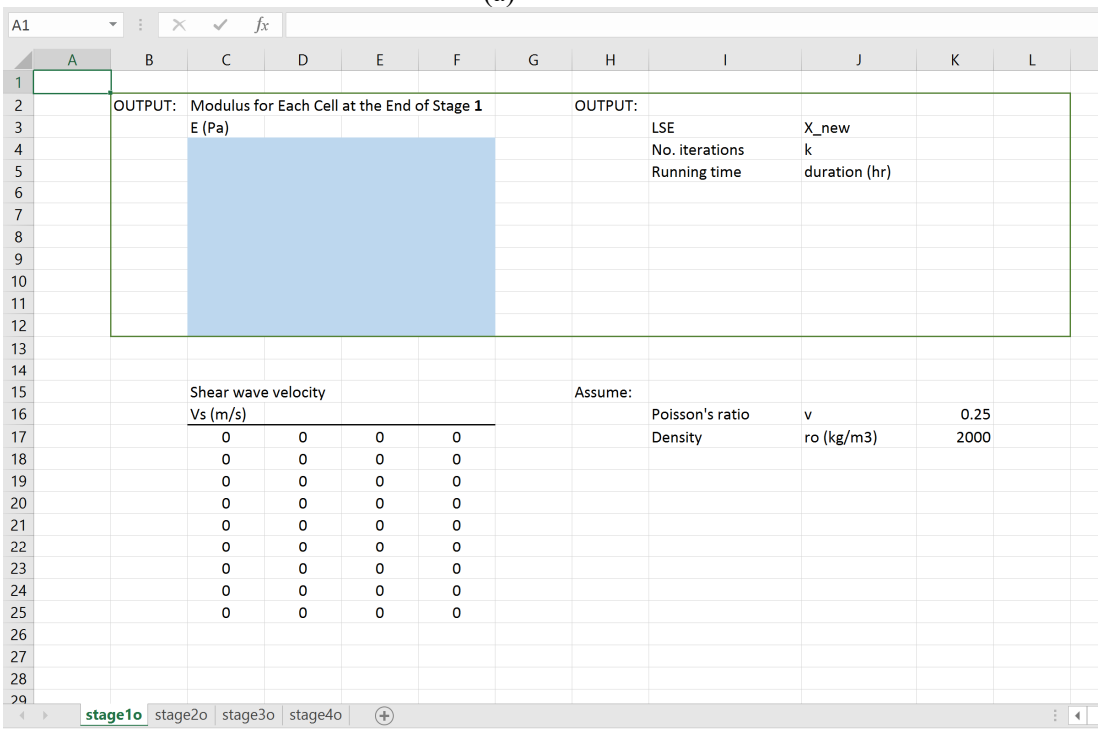

1											
2	OUTPUT:	Modulus for Each Cell at the End of Stage **1**					OUTPUT:				
3		E (Pa)						LSE	X_new		
4								No. iterations	k		
5								Running time	duration (hr)		
6											
7											
8											
9											
10											
11											
12											
13											
14											
15		Shear wave velocity					Assume:				
16		Vs (m/s)						Poisson's ratio	v	0.25	
17		0	0	0	0			Density	ro (kg/m3)	2000	
18		0	0	0	0						
19		0	0	0	0						
20		0	0	0	0						
21		0	0	0	0						
22		0	0	0	0						
23		0	0	0	0						
24		0	0	0	0						
25		0	0	0	0						
26											
27											
28											
29											

stage1o | stage2o | stage3o | stage4o

(b)

Figure 3-12 (a) Excel input sheet “stage1i” and (b) Excel output sheet “stage1o” for Step 1

3.5 Concluding Remarks

It is important to note that the ultimate purpose of the analysis software developed in this part of the study was to create an image of the material adjacent to a borehole using the data collected by the instrument (i.e., field measurements). These data will be the borehole sidewall motion versus time signatures recorded at each receiver position in the instrument, the so-called full waveforms. Herein, synthetic records have been used in the example simulation cases to demonstrate the imaging capability and the efficiency of the analysis software.

As it turns out, we have not had to develop a new forward model but have developed a revision of our original Abaqus model that can be run within the Student Version of Abaqus, which is available for no cost. In addition, our work has resulted in several performance improvements to our original system from the previous project.

It is anticipated that the analysis software and simulation procedure may need to be adapted once actual field data are acquired and used in the inversion process, as it is widely acknowledged that some noise exists in field measurements. These processes are demonstrated in Section 4.4 below using experimental full waveforms collected from the top surface of a synthetic limerock block specimen.

CHAPTER 4
TASK 3: VALIDATION EXPERIMENTS

4.1 Introduction

In Task 3, we conducted physical experiments using the borehole instrument to demonstrate the viability of the new test method. We built three lab-scale experimental models in which to test our borehole instrument. These specimens have been used extensively to investigate iterations of the instrument during development. We also used the boreholes at the Newberry field site to test both the low-frequency solenoid source and the barrel stave source with the 3D geophone string. The site is well known, and the northwest corner of the site has rock very near the ground surface to aid in the initial field investigation of the new test system.

4.2 Acrylic Tube

First, an acrylic tube borehole model was used to demonstrate that the piezoelectric source and amplifier can generate sufficient energy at high frequencies to be effectively measured by our inflatable membrane receiver array.

Figure 4-1 shows a first demonstration of the Kalinski-type inflatable bladder in an acrylic tube. One axial accelerometer is shown glued to the inside of the membrane and a small hammer was used to excite vibrations within the tube. The time and frequency domain records indicated that a credible waveform was measured by the accelerometer and that effective coupling of the accelerometer with the tube was made via the inflatable membrane.

Figure 4-2 shows a demonstration of a 14-kHz, 3.5-inch diameter piezocylinder that has been glued to the inside of an acrylic tube to imitate effective coupling with the borehole wall. An axial accelerometer is shown glued to the outside of the tube. The time and frequency domain records indicated that a credible waveform was measured by the accelerometer after the piezocylinder was excited with a short-duration electric pulse. The predominant response occured around the resonant frequency of the cylinder of 14 kHz. As intended, a cylinder effectively coupled to borehole wall generated strong vibrations along the axis of the borehole.

Figure 4-3 again shows a demonstration of a 14 kHz, 3.5-inch diameter piezocylinder that has been glued to the inside of an acrylic tube. In addition, the Kalinski-type inflatable bladder with one axial accelerometer glued to the inside of the membrane was inflated within the tube to couple the accelerometer to the inside wall of the tube. The time and frequency domain records indicate that a credible waveform is measured by the accelerometer after the piezocylinder is exited with a short-duration electric pulse. This simple experiment was the first successful demonstration of the basic concept of the project to measure a wavefield generated by a monopole, ring-type loading within a borehole using receivers coupled to the borehole wall.

Figure 4-4 shows a demonstration of a piezocylinder coupled to the inside of an acrylic tube with the inflatable canister and bladder system. In addition, the Kalinski-type inflatable bladder with one axial accelerometer glued to the inside of the membrane was inflated within the tube to couple the accelerometer to the inside wall of the tube. The time and frequency domain records indicate that a credible waveform is measured by the accelerometer after the piezocylinder is exited with a short-duration electric pulse. This experiment demonstrated the basic concept of a moveable and repeatable system for generating and measuring a wavefield within a borehole.

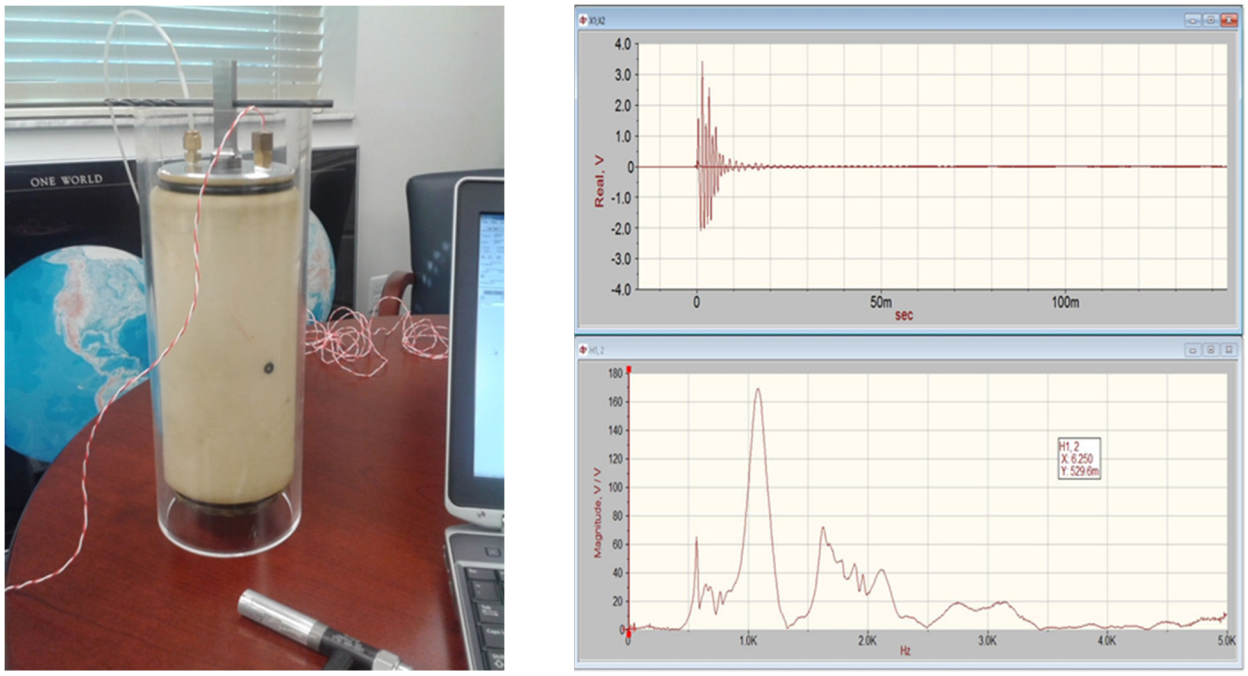

Figure 4-1 Demonstration of borehole receiver coupling system in acrylic tube

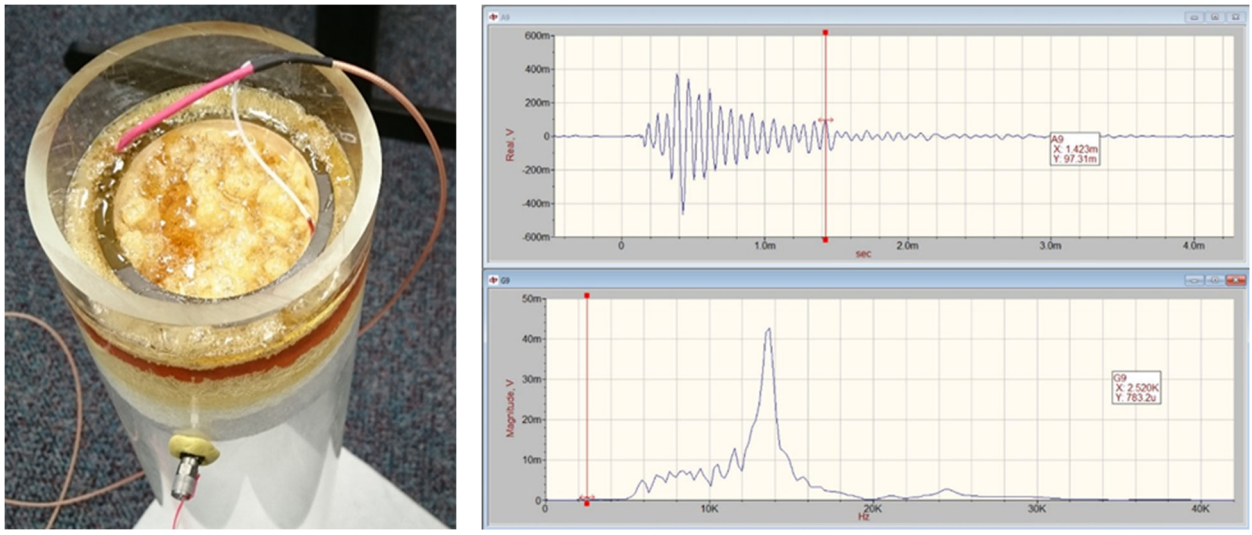

Figure 4-2 Demonstration of piezocylinder performance in acrylic tube

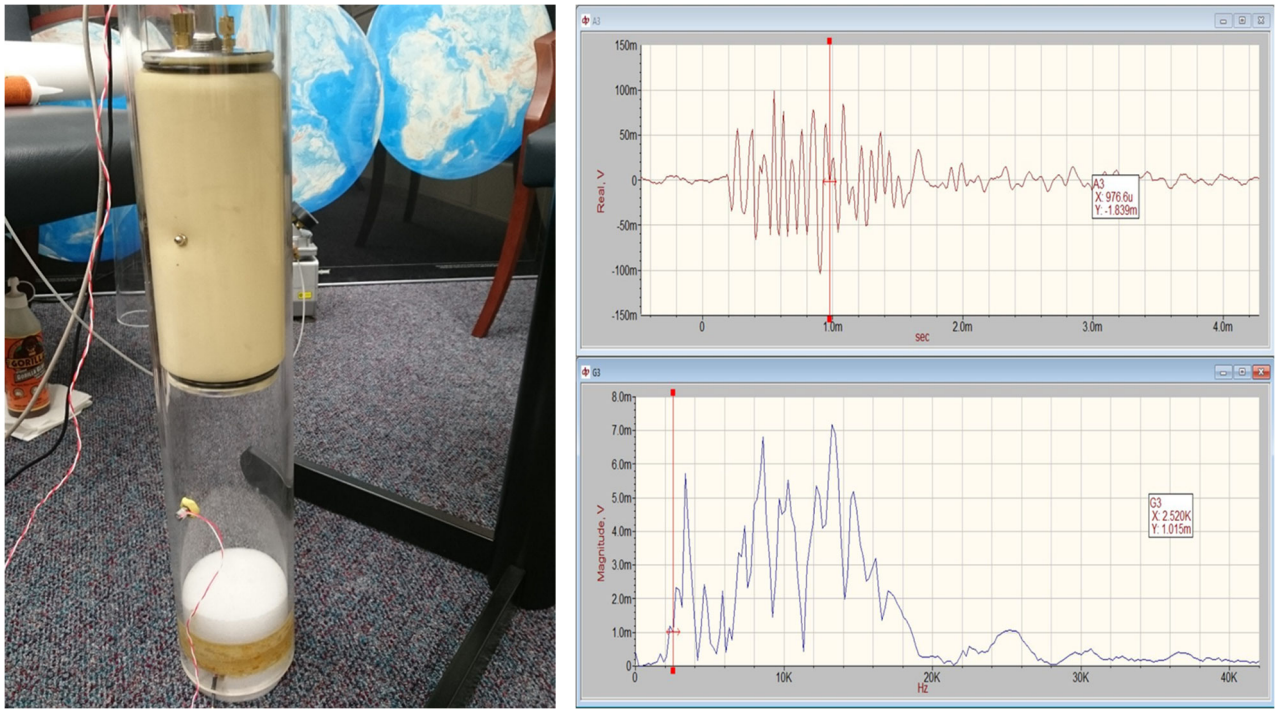

Figure 4-3 Demonstration of combined piezocylinder source and receiver coupling system in acrylic tube

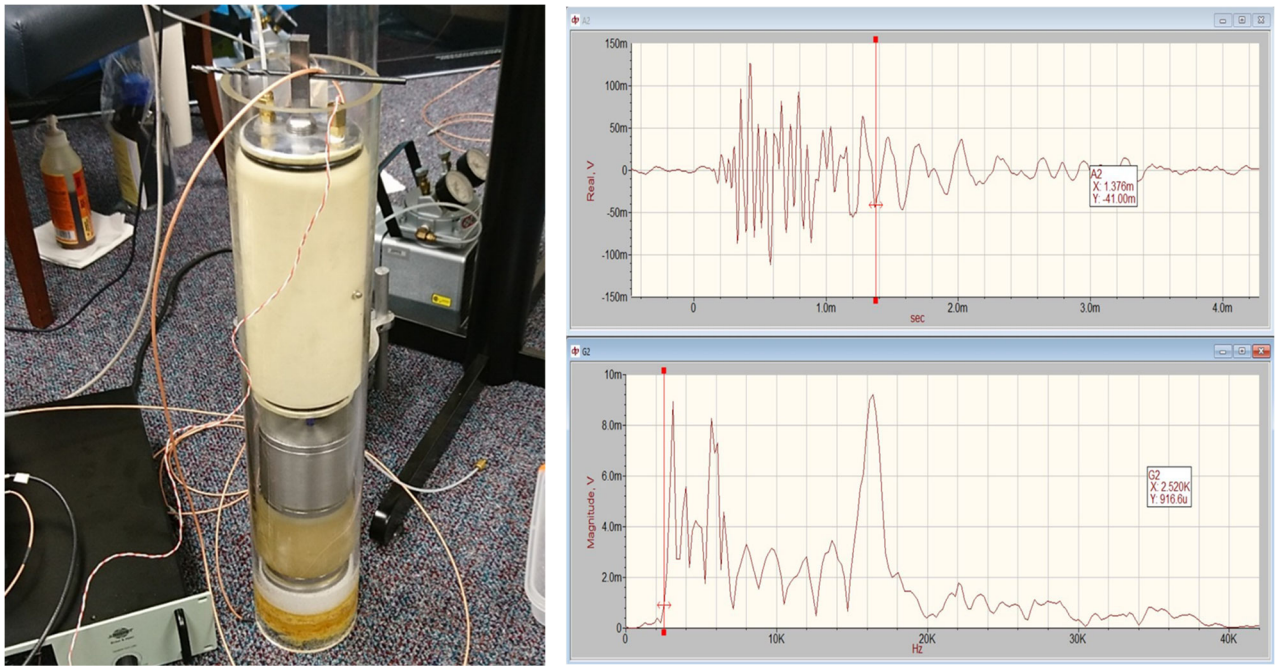

Figure 4-4 Demonstration of inflatable canister/piezocylinder with receiver coupling system in acrylic tube

4.3 Synthetic Limerock Cylinder

Second, we have built a cylindrical borehole model from synthetic limerock to demonstrate that the system concept does work with a more realistic material (limerock rather than acrylic). We have also used the cylindrical model for demonstrating an effective inflatable canister for implementing the piezoelectric cylinder source in a borehole.

Figure 4-5 shows a demonstration of a 14 kHz, 3.5-inch diameter piezocylinder that has been glued to the inside of a synthetic limerock cylinder to imitate effective coupling with the borehole wall. An axial accelerometer is shown glued to the inside of the cylinder on the opposite end. The time and frequency domain records indicate that a credible waveform is measured by the accelerometer after the piezocylinder is exited with a short-duration electric pulse. The predominant response occurs around the resonant frequency of the cylinder of 14 kHz. As intended, a cylinder effectively coupled to borehole wall can generate strong vibrations along the axis of the borehole.

Figure 4-6 again shows a demonstration of a 14 kHz, 3.5-inch diameter piezocylinder that has been glued to the inside of a synthetic limerock cylinder. In addition, the Kalinski-type inflatable bladder with one axial accelerometer glued to the inside of the membrane was inflated within the cylinder to couple the accelerometer to the inside wall of the cylinder. The time and frequency domain records indicate that a credible waveform is measured by the accelerometer after the piezocylinder is exited with a short-duration electric pulse. This simple experiment was a successful demonstration of the basic concept of the project to measure a wavefield generated by a monopole, ring-type loading within a borehole using receivers coupled to the borehole wall. In this case the wavefield is transmitted through a more realistic material (limerock rather than acrylic).

Figure 4-7 shows a demonstration of a piezocylinder coupled to the inside of a synthetic limerock cylinder with the inflatable canister and bladder system (top is visible). In addition, and not visible in the photograph, the Kalinski-type inflatable bladder with one axial accelerometer glued to the inside of the membrane was inflated within the cylinder to couple the accelerometer to the inside wall of the cylinder below the piezoelectric source. The time and frequency domain

records indicate that a credible waveform is measured by the accelerometer after the piezocylinder is exited with a short-duration electric pulse. This experiment again demonstrated the basic concept of a moveable and repeatable system for generating and measuring a wavefield within a borehole. In this case the wavefield is transmitted through a more realistic material (limerock rather than acrylic).

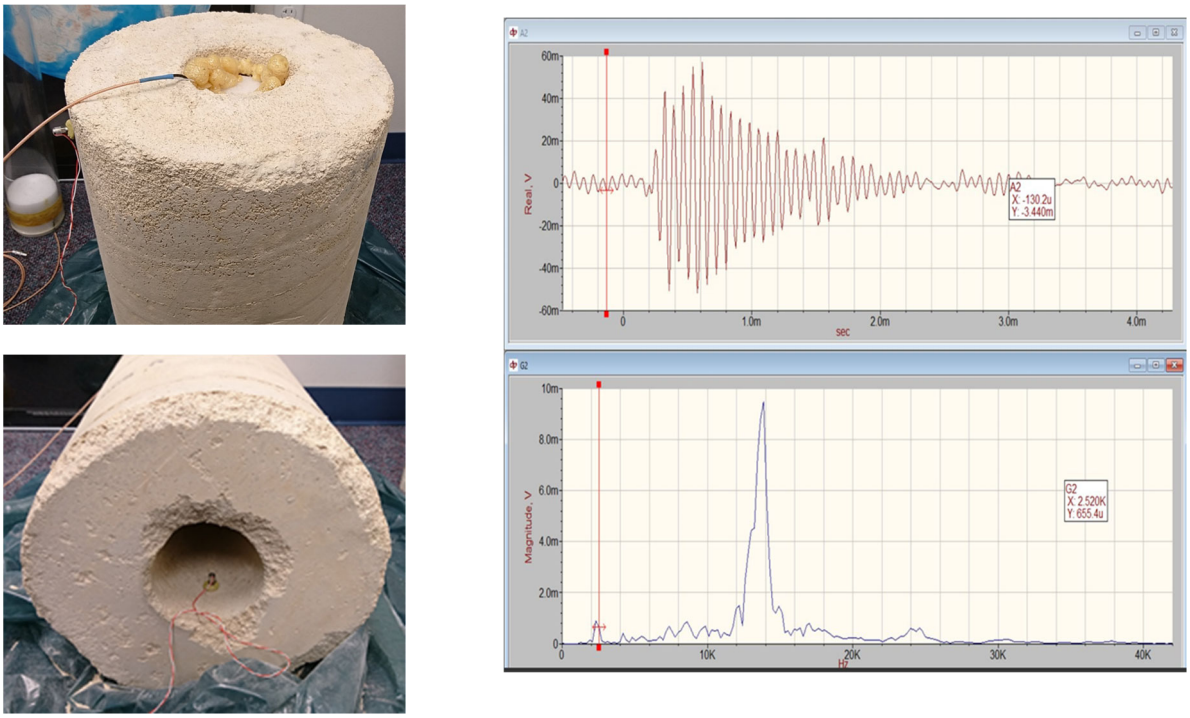

Figure 4-5 Demonstration of piezocylinder performance in synthetic limerock cylinder

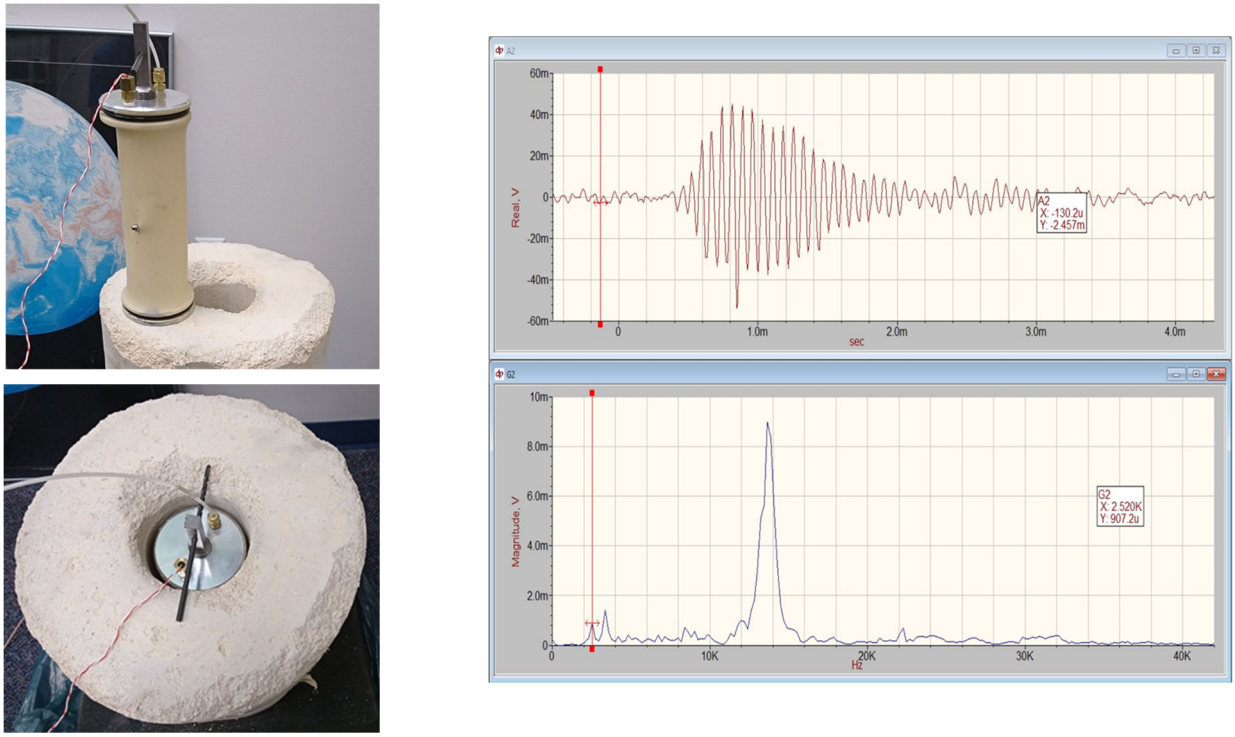

Figure 4-6 Demonstration of combined piezocylinder source and receiver coupling system in synthetic limerock cylinder

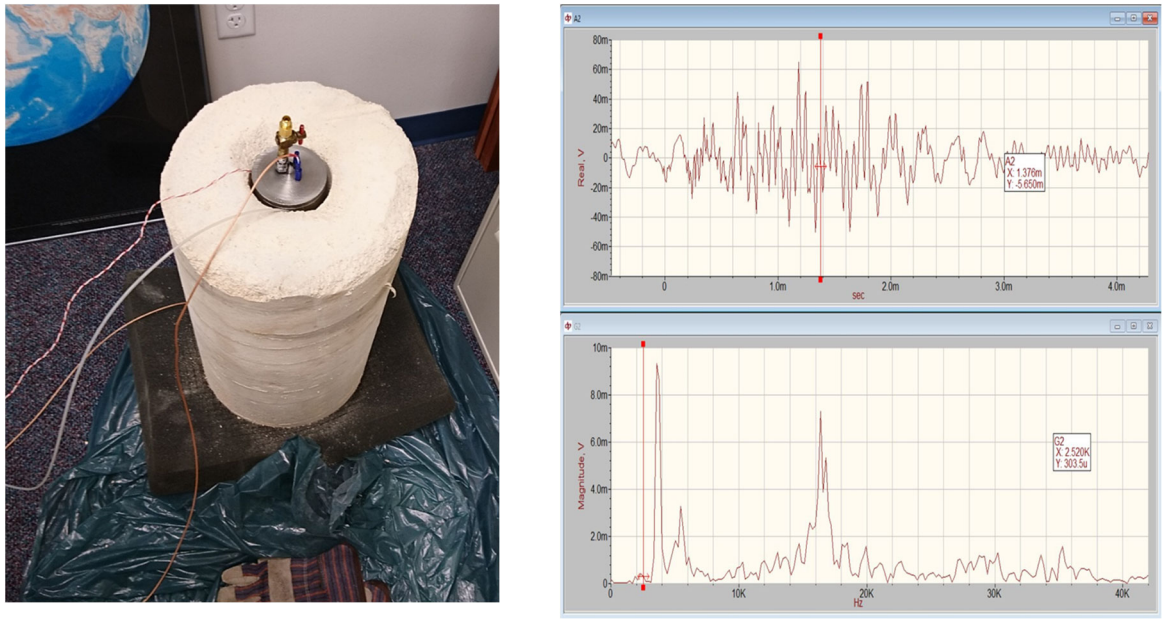

Figure 4-7 Demonstration of inflatable canister/piezocylinder with receiver coupling system in synthetic limerock cylinder

4.4 Top Surface of Synthetic Limerock Block

4.4.1 Introduction

Third, we have built a 1-meter cubical model with borehole from synthetic limerock. To date, we have used the top flat surface of the cube to collect realistic full waveform signals from which we have learned how to process these records effectively for use in the Inversion Software.

To date, no full waveform inversion has been conducted on Florida limerock-like material and this experiment was our first attempt to investigate the feasibility using a specimen whose modulus properties can be independently verified. As well, the experiment provided an opportunity to develop appropriate strategies for effectively processing full waveforms, including choice of motion component to invert (i.e., acceleration, velocity, or displacement) and types of temporal and frequency filtering.

A laboratory specimen one cubic meter in size was employed for purpose of this study. The cubic specimen was made of low-strength concrete (synthetic limerock) and included a through borehole (0.1 m in diameter) at the center, as shown in Figure 4-8. Since the equipment/source for generating the required seismic waves (down the borehole) was still under development, an alternative source, i.e., a hammer was used to apply a pulse load at one corner of the top surface of the concrete cube. The resulting accelerations were recorded using a string of ten receivers placed along the diagonal line of the top surface (Figure 4-8). The receivers were spaced evenly at a distance of 0.05 m with the first one placed 0.08 m away from the source. Multiple tips can be used along with the hammer to apply the load. This study analyzed data induced by two tips, i.e., a plastic tip (black) and a metal tip (white). The measured record associated with the plastic tip was used herein to demonstrate the complete process of full waveform inversion, including raw data analysis, forward modeling, and inversion.

Figure 4-8 Laboratory testing of a concrete (synthetic limerock) specimen

4.4.2 Analysis of Measured Data

Figure 4-9 shows time record of the source (plastic tip), i.e., a concentrated pulse load applied to the concrete cube during the laboratory test. The load had a peak value of 262.6 N and lasted for approximately 3 ms. Complete acceleration data measured at the ten receivers are presented in Figure 4-10(a). Although the record of acceleration were over 60-ms long, most activities (significant values) occurred within the first 6 ms.

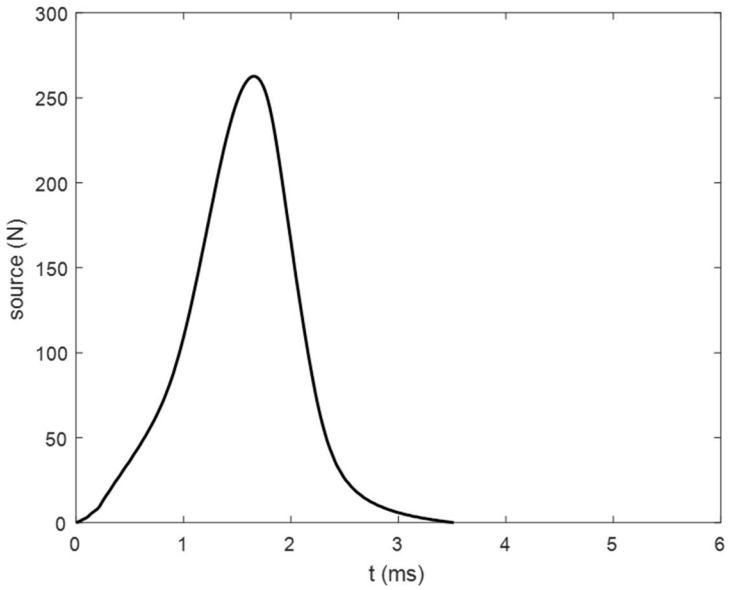

Figure 4-9 Concentrated pulse load recorded during the laboratory test

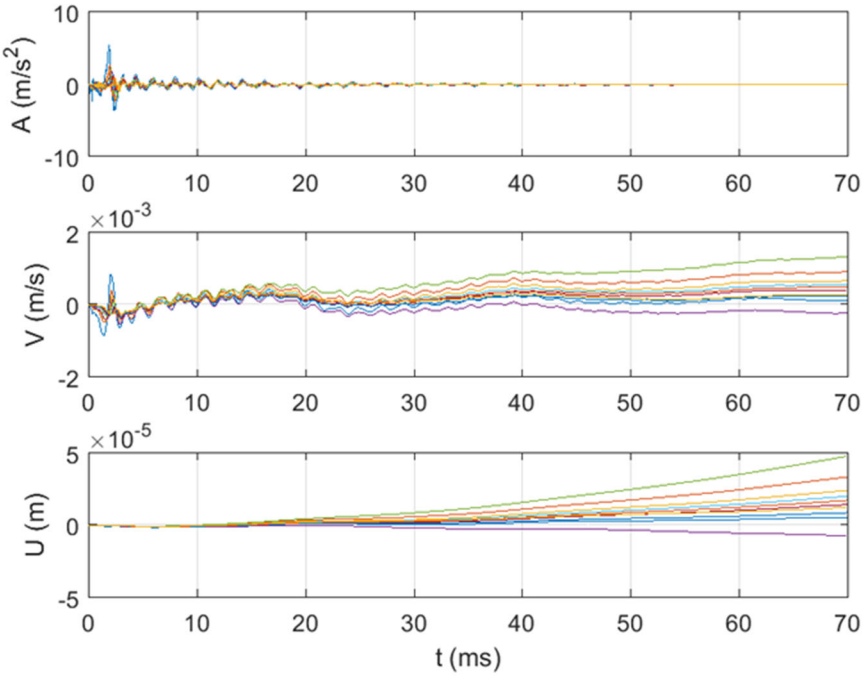

Figure 4-10 Measured acceleration transformed to velocity and displacement through time integration without high-pass filtering (complete time records)

Figures 4-10(b) and 4-10(c) show erroneous velocity and displacement results, respectively. These were obtained from numerical integration of the measured acceleration data without high-pass filtering. This type of error is commonly referred to as “data drift”. To avoid its occurrence, the acceleration data were filtered using a high-pass filter before being transformed to velocity and displacement through time integration. Figure 4-11(a) shows complete time records of the corrected velocity and displacement results along with the high-pass filtered acceleration data. Figure 4-11(b) provides a close-up of the data by zooming into time records of the first 6 ms. The acceleration was in the range of -4 to 6 m/s^2 and the velocity was in the range of -1 to 1 mm/s. The displacement was in the range of -1.5 to 1 μm/s, which can be better viewed in Figure 4-11(a).

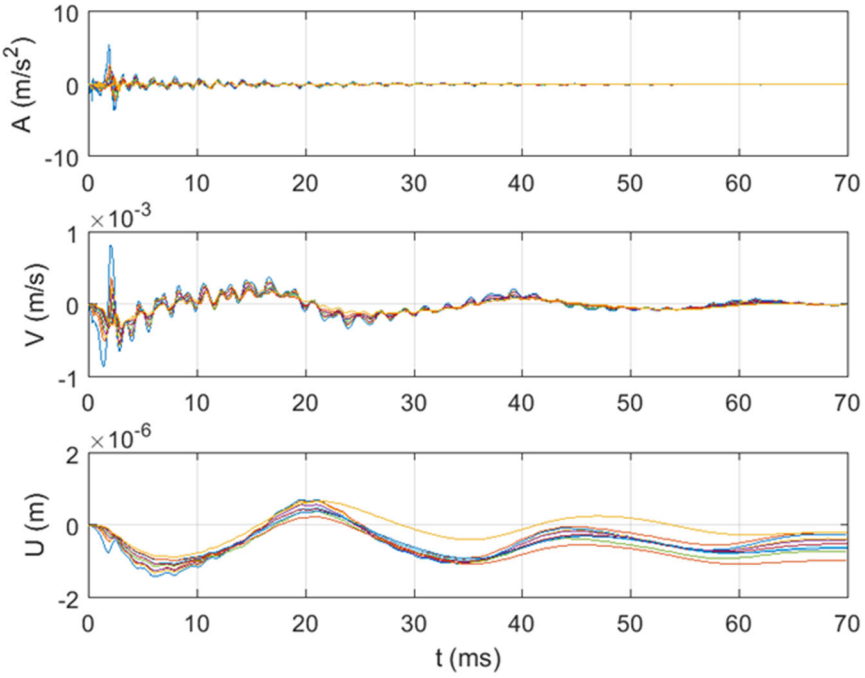

(a) Complete time records

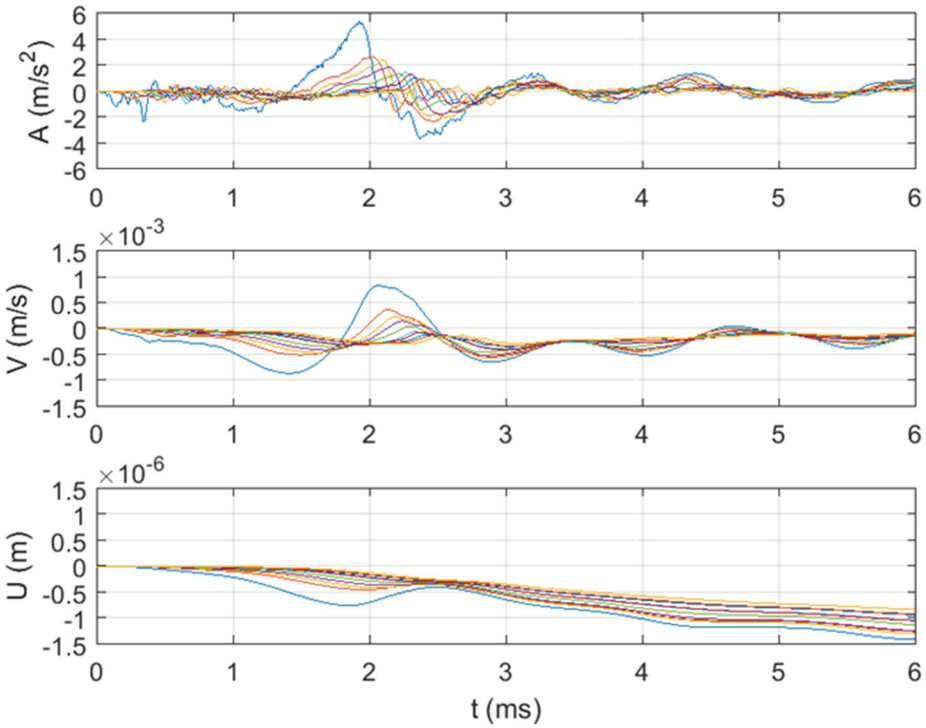

(b) First 6-ms data sets

Figure 4-11 Measured acceleration transformed to velocity and displacement through time integration with high-pass filter

4.4.3 Forward Modeling Using Finite Element Method

This study uses ABAQUS, a general-purpose finite element package, to model the propagation of seismic waves inside the concrete cube. Measured source data were applied to the concrete cube in forward modeling to simulate the actual loading condition. A dynamic explicit analysis procedure was employed to solve the wave propagation problem. The analysis time was set to be 6 ms, which is about two times the duration of the source load.

For reduced computing time, the three-dimensional concrete cube was represented using an axisymmetric model. The size of the model was determined based on the premise that no reflective waves should arrive at the receivers during the 6-ms analysis time. Given the compressive wave velocity of the concrete material (1,500 m/s) obtained from the free-free

resonance column test, the size of the model was obtained to be 4.53 m (Figure 4-12). The material of the concrete cube was assumed to be linear elastic with the following properties:

- Mass density = 2,150 kg/m^3
- Poisson's ratio = 0.2
- Young's modulus = 4.35 GPa

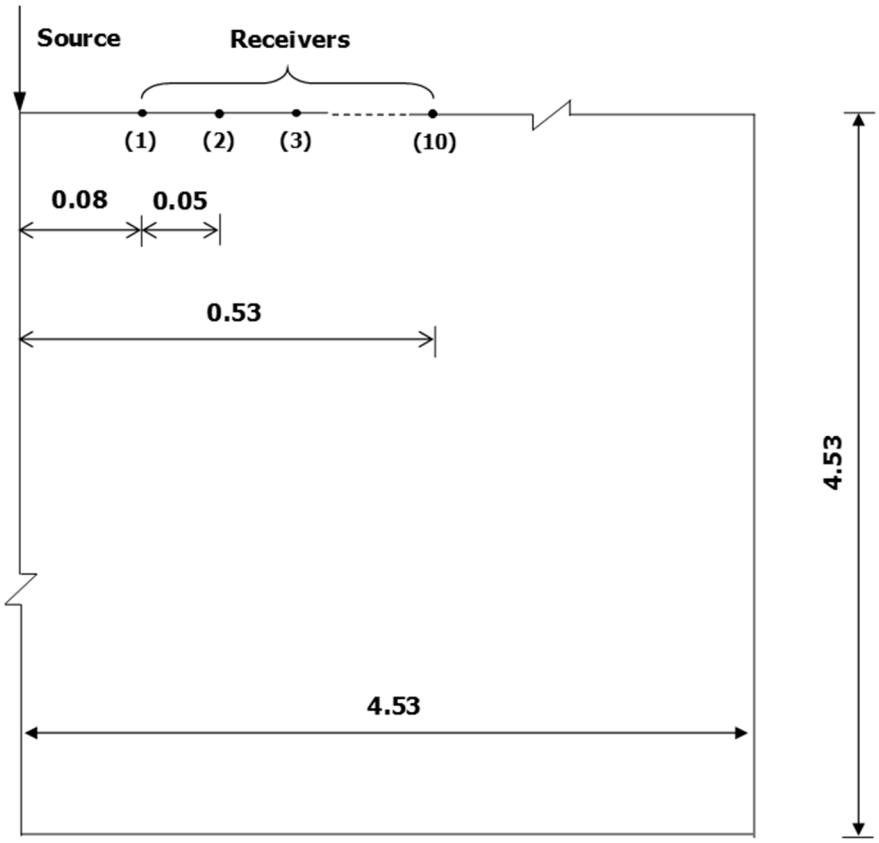

Figure 4-12 Axisymmetric FE model created for the concrete block (all sizes in meter)

A 4-node reduced integration element type (CAX4R) was selected to create a finite element mesh of the model. Enhanced hourglass control was employed to minimize mesh instability (commonly referred to as "hourglassing"). According to ABAQUS (2013), the element size for the model should be no greater than 0.45 m. In this study, the element size was controlled by the receiver spacing (0.05 m) and the spacing between the first receiver and the source (0.08 m). It was determined to be 0.01 m to allow for a minimum of five elements between every two receivers. The resulting finite element mesh had about 205,000 elements.

For a dynamic explicit finite element analysis, response (output) of a model is typically requested for every time increment. This time increment is called stable time increment in ABAQUS, which is determined based on the highest frequency response of the model. The stable time increment parameter has a smaller size for the first a few increments and then reaches a stabilized value (ABAQUS, 2013). The maximum output sampling rate is determined as the inverse of the stabilized time increment. For the concrete cube model, the stabilized time increment was 5.8E-6 s and the corresponding maximum output sampling rate was about 200 kHz.

It is important to note that acceleration and force results recorded at the maximum output sampling rate involve high-frequency solution noise in addition to lower-frequency structural response that we want to obtain. Therefore, low-pass filtering is necessary to remove the high-frequency solution noise. The highest frequency of structural response is typically two orders of magnitude lower than the highest frequency of the model (overall response).

For the concrete cube model, the highest frequency of the model was about 100 kHz, which was determined as half of the maximum output sampling rate (Nyquist Theorem). The highest frequency of structural response was 1 kHz or lower. In this study, a built-in anti-aliasing low-pass filter, namely second-order Butterworth filter, was employed to remove the high frequency solution noise before the signal was sampled (ABAQUS, 2013). An initial cutoff frequency of 8 kHz was used to avoid over-filtering. The cutoff frequency of the filter was then reduced to identify the optimum value that would achieve the best match between the predicted and measured acceleration data.

Through a trial-and-error process, a cutoff frequency of 4 kHz was selected to produce the finite element results. For the cutoff frequency to be 4 kHz, the output sampling rate should be at least 24 kHz (calculated as 6 times 4 kHz according to ABAQUS, 2013). Therefore, an output sampling interval of 4E-5 s, corresponding to the sampling rate of 25 kHz was used to request the finite element output.

Figure 4-13 shows the resulting acceleration, velocity, and displacement time signatures predicted at the locations of the ten receivers for a period of 6 ms. Overall, the finite element results agreed well in shape with the measured ones presented in Figure 4-11(b). Only slight overestimation was observed. The difference was expected because one quarter of a cylinder modeled in the simplified finite element analysis was not the exact representation of the concrete cube. As mentioned earlier, the simplification in forward modeling was aimed at achieving a great saving in computing time during the full waveform inversion process, which requires multiple iterations to convergence. Furthermore, the small difference in magnitudes will not cause problems for inversion because responses in a normalized form are used to achieve the best-fit match in the inversion routine described in the next section.

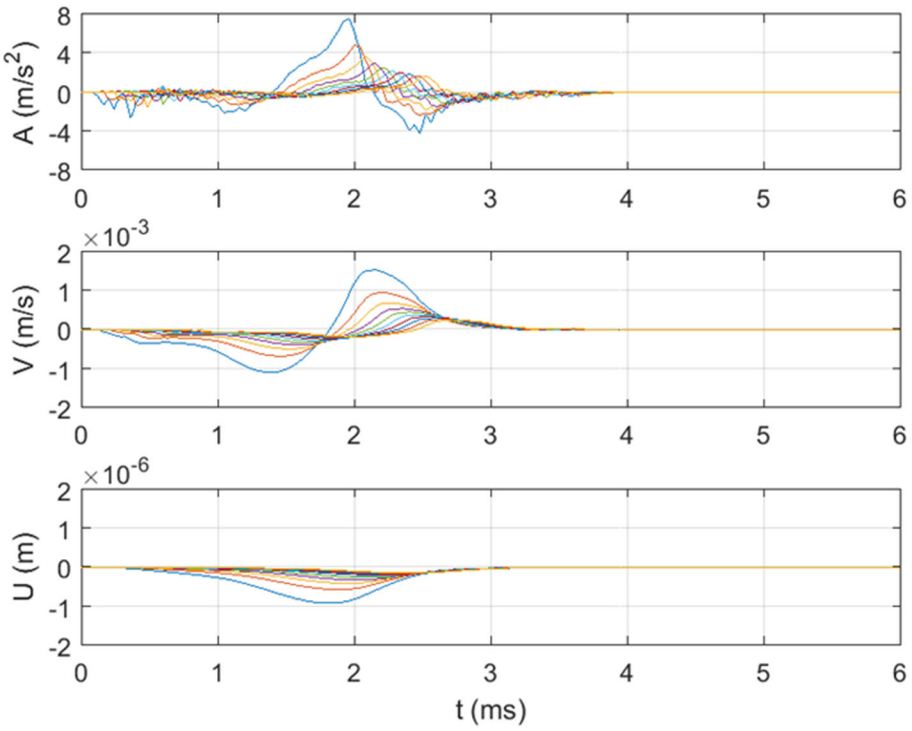

Figure 4-13 A, V, U results (6 ms) predicted by the axisymmetric FE model

4.4.4 Inversion Using Regularized Gauss-Newton Method

An inversion routine was developed to find the optimal shear wave velocity values that produce a best-fit match between measured and predicted structural responses. The inversion routine used

a regularized Gauss-Newton iteration algorithm described by Hiltunen and Jiang (2013) and Sheen et al. (2006).

The axisymmetric finite element model described earlier was used as a forward model for the inversion. In essence, the shear wave velocity of the concrete cube model was systematically adjusted until a best-fit match was achieved between measured and predicted responses, including displacements, velocities, and accelerations. It should be noted that the actual size of the concrete cube used in the laboratory test was 1 m. Given the compressive wave velocity of the concrete material (1500 m/s), the wave was estimated to hit the boundary of the cube after traveling for about 0.6 ms. Therefore, only the first 1.2 ms time records of responses were used in the inversion process to eliminate the effect of reflected waves. Furthermore, since axisymmetric assumption becomes unsuitable when the receivers get closer to the central borehole (Figure 4-8), only the waveforms obtained at the first three receivers were used in the inversion.

Figure 4-14 presents inversion results based on the best-fit match of normalized displacements. The inversion was set to run for 25 iterations and an initial shear wave velocity of 760 m/s was used. No low-pass filter was applied to the waveforms throughout the inversion process. Figure 4-14a shows that measured and predicted displacements were well matched after 25 iterations. During the inversion process, shear wave velocity increased gradually until it stabilized at 945 m/s (Figure 4-14b), while lease square error (LSE) decreased gradually and stabilized at 4.1E-5 (Figure 4-14c).

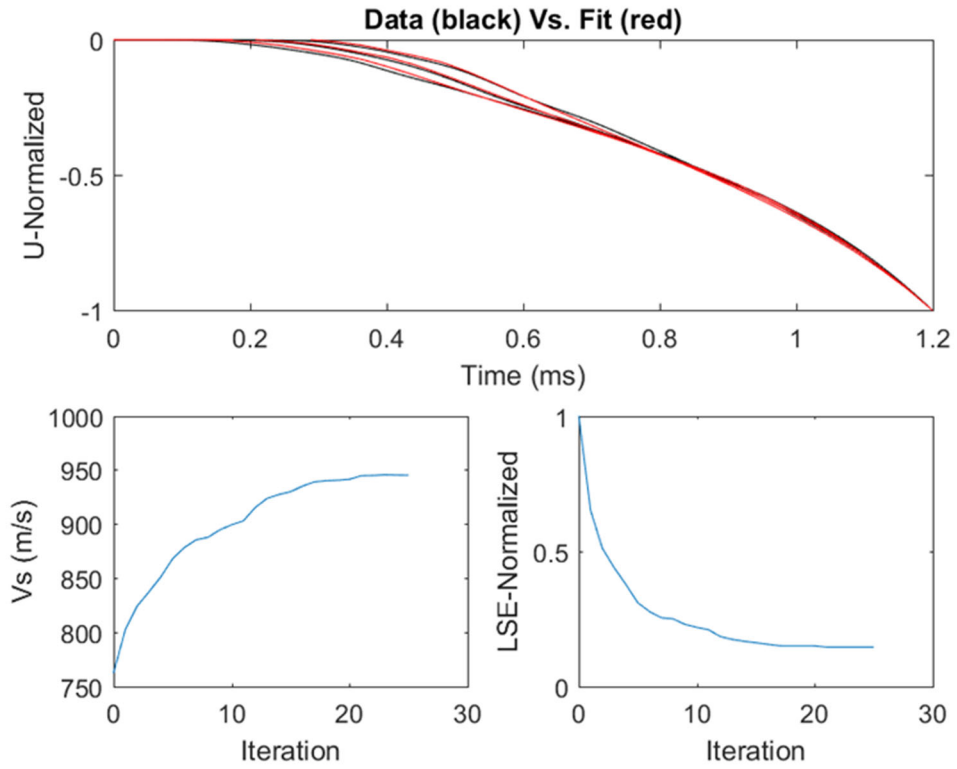

Figure 4-14 Inversion results by minimizing misfit in displacements (without filter)

Inversion results based on the best-fit match of normalized velocities and accelerations are shown in Figures 4-15 and 4-16, respectively. The same initial shear wave velocity and maximum number of iterations were used in the inversion process. Unlike the inversion based on displacements, one low-pass filter, which was necessary for convergence, was applied to the velocity and acceleration waveforms throughout the inversion process.

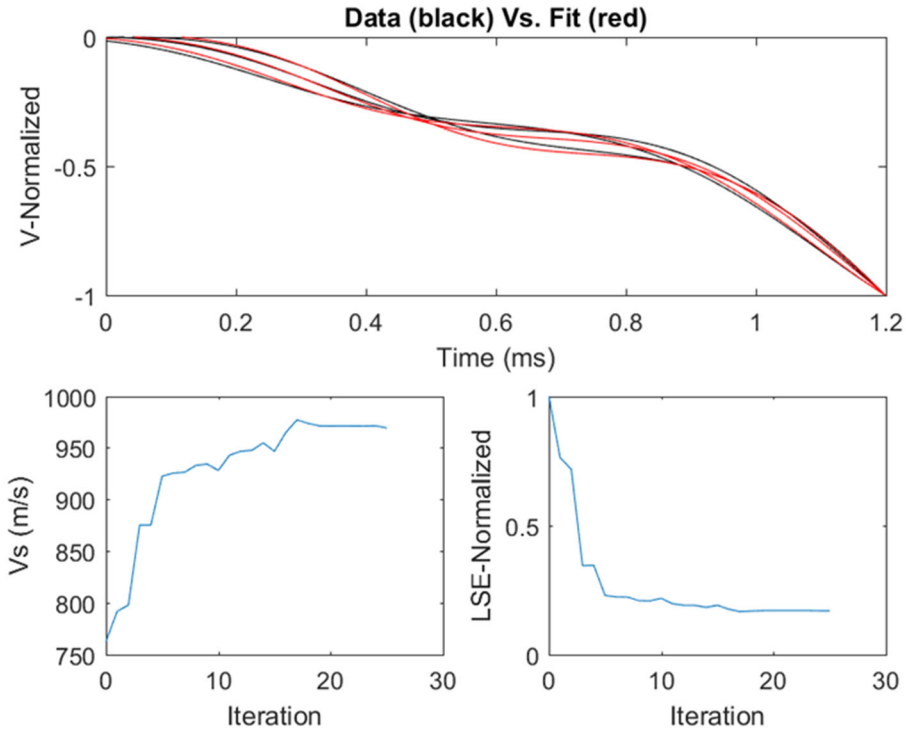

Figure 4-15 Inversion results by minimizing misfit in velocities (with low-pass filter)

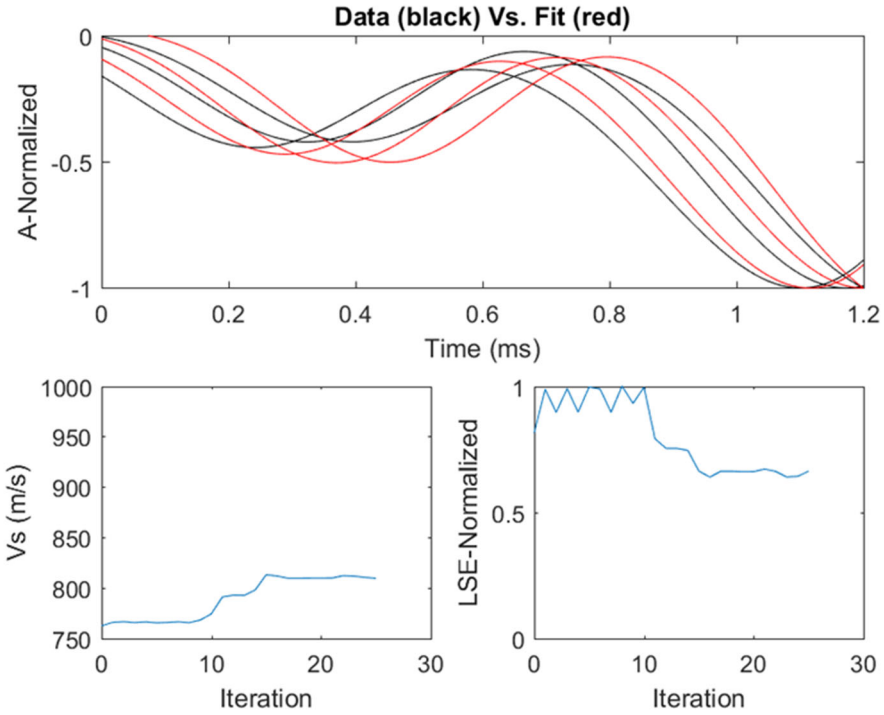

Figure 4-16 Inversion results by minimizing misfit in accelerations (with low-pass filter)

Figure 4-15a shows that measured and predicted velocity were matched reasonably well after 25 iterations. The convergence rate was very fast for the first five iterations, leading to a shear wave velocity of 925 m/s (Figure 4-15b). Almost no change occurred in the LSE after about five iterations (Figure 4-15c). It appeared that the inversion results based on velocities ranged between 925 to 970 m/s at the LSE of 1.9×10^{-4}. Figure 4-16a shows that measured and predicted acceleration did not match after 25 iterations. Given the extremely slow convergence rates in both shear wave velocity and LSE (figures 4-16b and 4-16c), the acceleration data was determined unsuitable for inversion.

Overall, the inversion results based on normalized displacements were found most credible due to the lowest LSE achieved. Furthermore, no low-pass filter was needed throughout the inversion process. Therefore, the shear wave velocity was determined to be 945 m/s for the concrete cube, which was comparable to the true value (920 m/s) calculated from the measured compressive wave velocity (1,500 m/s).

4.4.5 Concluding Remarks

Laboratory experiments were conducted on a large-size concrete cube to demonstrate the viability of an analysis software to model material properties from actual measurement data. A summary of findings based on results of tests and analyses is presented as follows:

- Raw acceleration data should be filtered with a high-pass filter before being transformed into velocity and displacement through numerical integration, so that occurrence of "data drift" can be avoided.
- Axisymmetric finite element model representation can be used to simulate responses of a concrete cube under corner loading for reduced computing time, which provides forward models practical for full waveform inversion.
- For given simulation time (typically selected as a few times of loading duration), an appropriate model size should be determined accordingly to avoid receiving waves reflected from the model boundary.
- A run-time low-pass filter was necessary to remove high-frequency solution noise from acceleration responses before the signal was sampled. For the concrete cube model, the cutoff frequency of the filter was determined to be 4 kHz.

- Inversion results based on the best-fit match of normalized displacements were found to be most credible due to the lowest LSE achieved. For the concrete cube specimen, the shear wave velocity was determined to be 945 m/s.

4.5 Newberry Field Site

4.5.1 Low-Frequency Pneumatic Solenoids

We have conducted a field test using the PVC-cased boreholes at the Newberry field site to demonstrate the low-frequency solenoid source with the 3D geophone string. This was our first field implementation of generating a wavefield using a source and receiver array from within a single borehole.

Figure 4-17 shows the setup of the equipment. First, the geophone string was lowered into and then coupled to the inside wall of the borehole using an inflated firehose. The first 3D geophone pod was placed at approximately 0.5 m below the ground surface and the remaining seven geophone pods are along the string at a fixed spacing of 1 m. Thus, the array extends from depths of 0.5 m to 7.5 m below the ground surface. Next, the borehole source was attached to an aluminum orientation rod and lowered into the borehole. The striker plate on the source was located at a depth of approximately 0 m, i.e., the ground surface. We did not lower the system any further during this first trial since the current setup has some cable size issues that led to cramping of the equipment in the borehole; we did not want to risk getting the source stuck in the borehole beyond immediate reach. We intend to modify the setup for future use to enable confident access throughout the borehole length (about 17 m).

Figure 4-18 shows the time records from all 24 geophones in the string and grouped by the direction of motion detected by the geophone for one strike of the solenoid source in the north-south direction. On the top left are the 8 records for motion in the horizontal direction, while the top right are the 8 records for motion in the horizontal direction perpendicular to the previous set. On the bottom are the 8 records for motion in the vertical direction. Within each group, receiver 0 corresponds to the geophone at a depth of 0.5 m, with each subsequent receiver at 1-m depth intervals. Our purpose in this first trial was simple: can credible vibration records be obtained

along the length of the receiver array with this setup? It appears that all time records are credible in this case and indicates the borehole solenoid source can produce a sufficient wavefield that can be measured throughout the length of the 3D geophone array. Our next steps are to modify the source and cabling system to allow unrestricted access to the complete length of the borehole and to test a new 3D waveform and inversion algorithm currently under development to analyze the data produced by this test setup. A true 3D analysis system is required since the solenoid source produces a dipole-type point load in the horizontal direction within the borehole.

Figure 4-17 Setup of low-frequency solenoid source and 3D geophone string at Newberry site

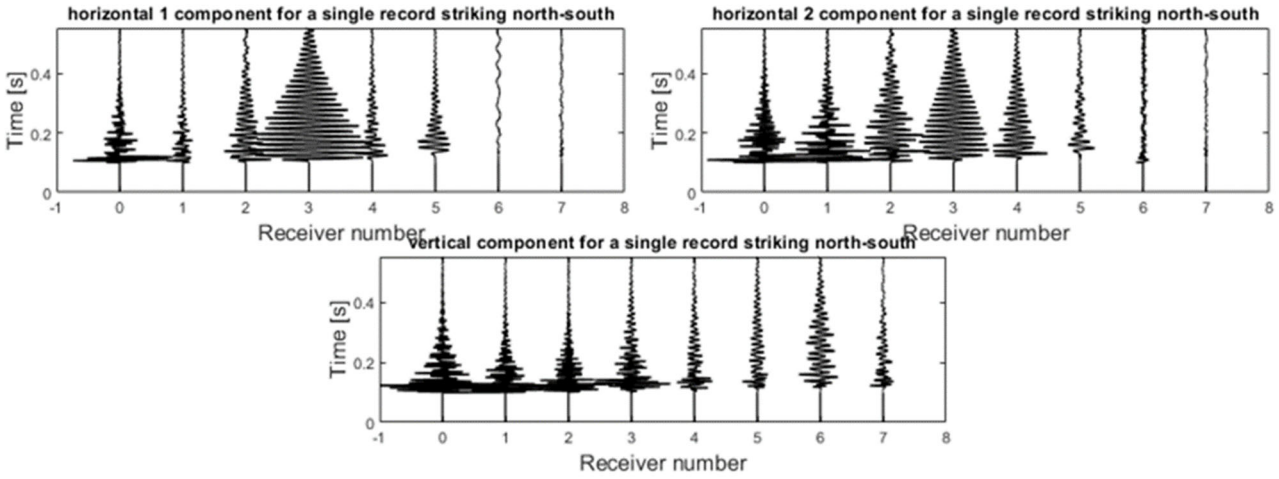

Figure 4-18 Time records from 3D geophone string at Newberry site

4.5.2 Mid-Range Barrel Stave Flextensional Transducer

Next, we have conducted a field test using the PVC-cased boreholes at the Newberry field site to demonstrate the barrel stave source with the 3D geophone string. To begin, we first mounted an accelerometer directly to the outside of the transducer to demonstrate its mechanical vibration characteristics (Figure 4-19). In this demonstration, an 80 V pulse was delivered to the transducer and the time and frequency response of the accelerometer is shown. The source can receive an input voltage in excess of 1 kV, thus this demonstration utilized less than 10% of the source capability. Nevertheless, a significant vibration was measured by the attached accelerometer, particularly near the first resonance of the source (around 2.5 kHz in air).

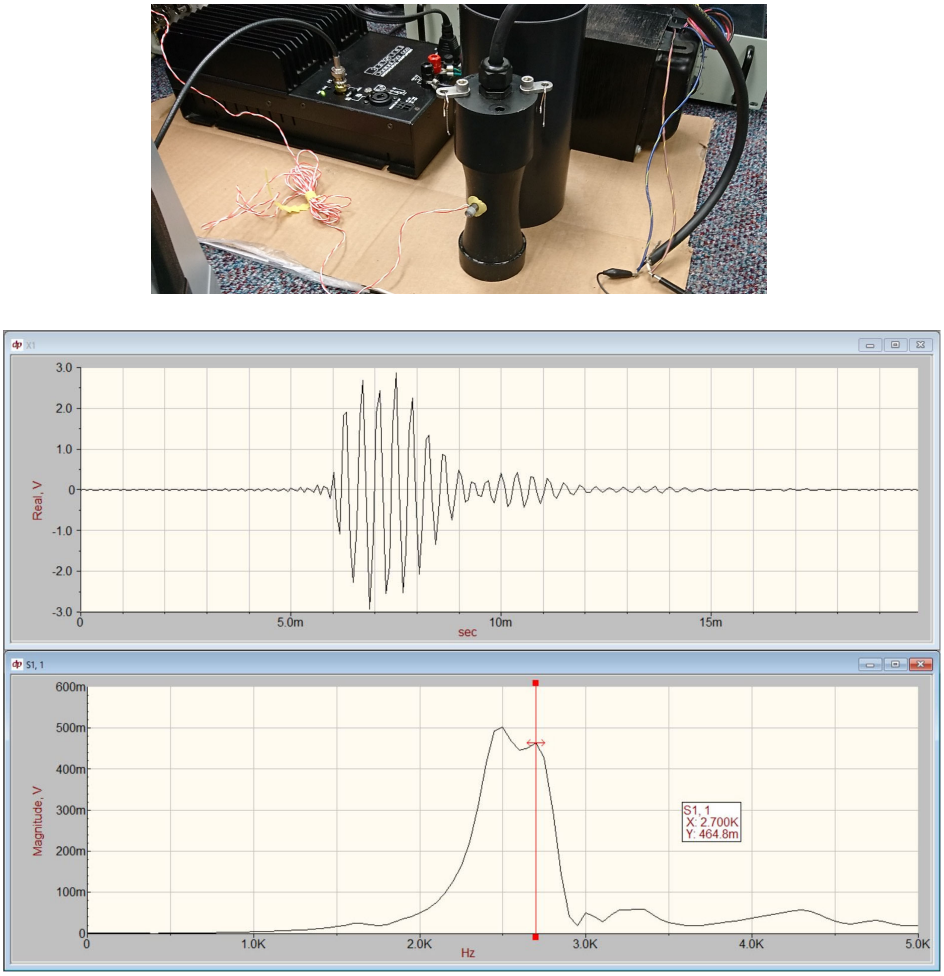

Figure 4-19 Demonstration of barrel stave source vibration in air

Next, we placed the source within a water-filled plastic cylinder and mounted an accelerometer on the outside of the cylinder to demonstrate its mechanical vibration characteristics as coupled through a fluid, as would be done in a fluid-filled borehole (Figure 4-20). Again, an 80 V pulse was delivered to the transducer and the time and frequency response of the accelerometer is shown. Despite using less than 10% of the source capability, a significant vibration was measured by the attached accelerometer, particularly near the first resonance of the source (around 1.8 kHz in water).

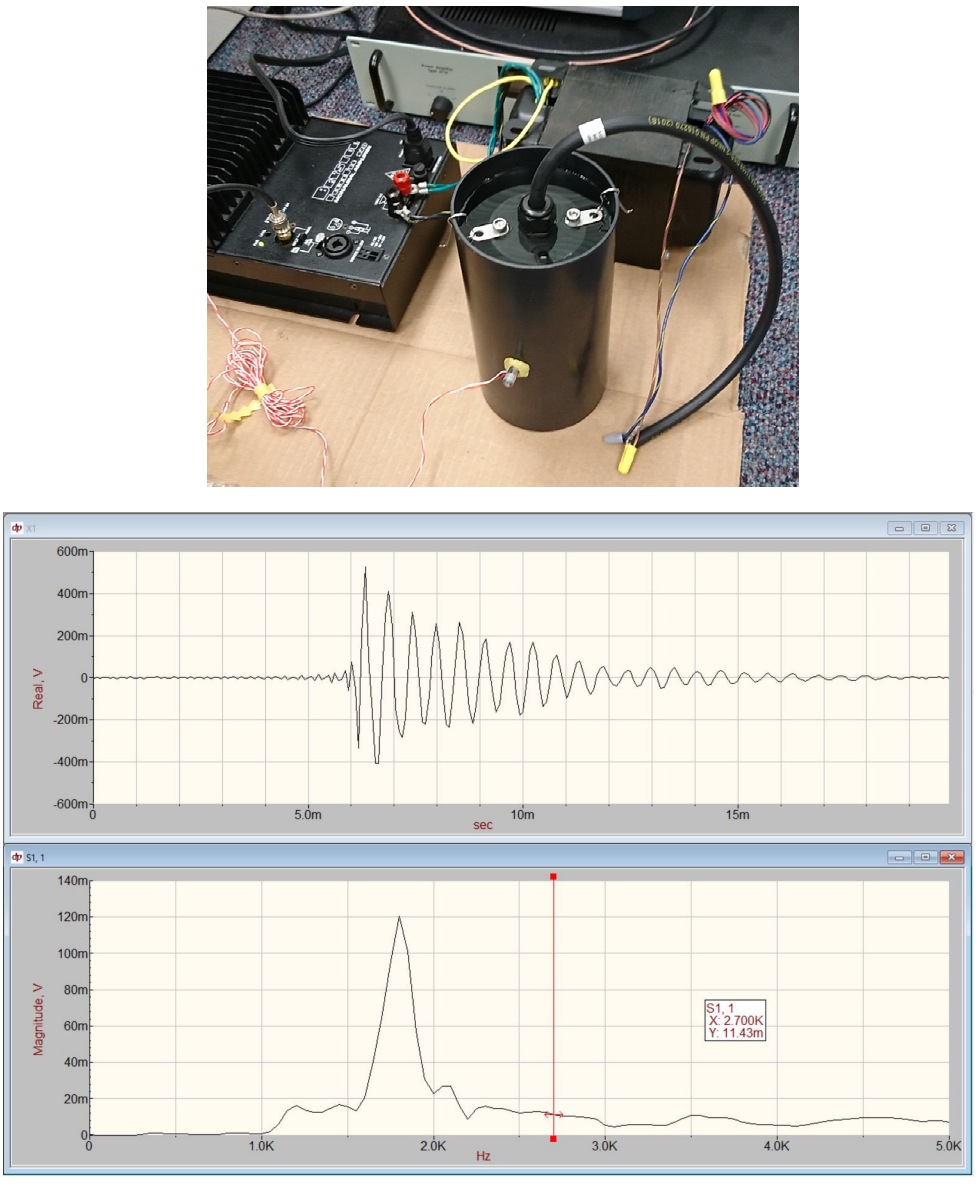

Figure 4-20 Demonstration of barrel stave source vibration in water

In a third setup (Figure 4-21), we attached the source to the eyelet at the end of the 3D geophone string (1 m below the 8th and last geophone pod on the string) and lowered the source and receiver array into the PVC-cased borehole noted in the photograph to a depth of 5 m below the ground surface. The water level in the borehole was found to be approximately 4 m below ground, thus the source was in water and four of the geophone pods were coupled with the inflatable fire hose to the borehole wall while the remaining four pods laid on the ground surface. Unfortunately, this demonstration revealed a shortcoming of the cabling system for the geophone string: the cable does not have enough electrical shielding from outside energy sources. When the high-voltage signal is sent to the source, the electrical signal from the source cable is coupled to the unshielded cable for the geophones, i.e., the geophone cable acts like an antenna. The coupled signal is large and completely masks any of the signal transmitted by the geophones when mechanically shaken. For any future applications a grounding system for both the source and geophone cables needs to be developed to achieve isolation.

Figure 4-21 Barrel stave source coupled to end of 3D geophone string

In an attempt to at least demonstrate that the source can generate a measurable wavefield in proximity to the borehole, we attached an accelerometer to the top inside wall of the PVC casing (near the while label in Figure 4-22) and excited the source with a 400 V, 1.5 kHz sine wave. The source remained in the borehole below water and at a depth of 5 m. As shown, even at nearly 6 m away, a measurable vibration was registered by the accelerometer. It is recommended that in future experiments, the source be paired with the Kalinski-type bladder and 3D accelerometer to produce a dataset for use in the inversion software. As of this writing, the bladder system and accelerometer were not yet ready for use below water.

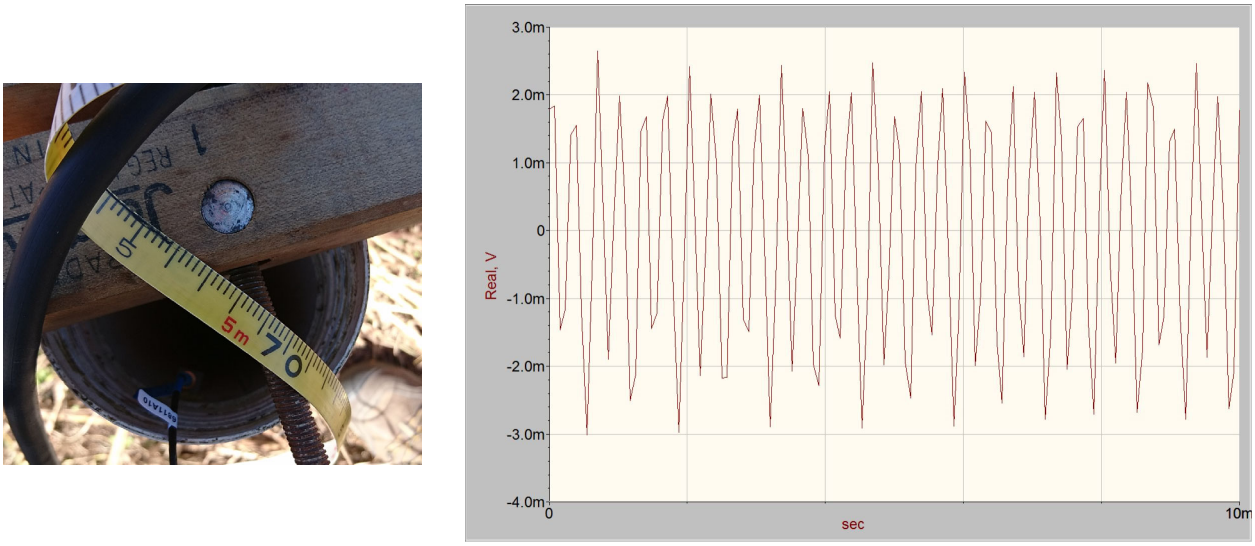

Figure 4-22 Demonstration of barrel stave source vibration in cased borehole

CHAPTER 5
CLOSURE

5.1 Summary of Findings

The objective of the project was to produce a prototype instrument and software analysis system for conducting geophysical characterization of subsurface conditions from within a single borehole. In Task 1, Borehole Instrument, two piezoelectric sources were constructed, the first using high frequency piezocylinders and the second using a barrel stave flextensional transducer. A third low frequency source using pneumatic solenoids was also investigated. For receivers, a system was constructed for coupling accelerometers to the wall of a borehole, and an existing 3D string of geophones was also investigated. In Task 2, Inversion Software, an analysis software was developed to create an image of the material adjacent to a borehole using the measurements from the borehole instrument and full wave inversion (FWI) technology. In Task 3, Validation Experiments, we built three lab-scale experimental models in which to test our borehole instrument. These specimens were used extensively to investigate iterations of the instrument during development. We also used the boreholes at the Newberry field site to test both the low-frequency solenoid source and the barrel stave source with the 3D geophone string.

5.1.1 Borehole Instrument

- An inflatable canister for repeatedly coupling a pair of piezocylinders wired in parallel inside an inflatable membrane was constructed and this canister system tested well in our small-scale experiments. However, we discovered from these experiments that the piezoelectric cylinders typically available from manufacturers do not generate the frequency content most desired for our borehole source.
- As an alternative configuration to the piezocylinders, a so-called piezoelectric barrel-stave flextensional transducer was configured for frequencies below 10 kHz. The barrel-stave element is driven by a commercially available power amplifier and transformer pair. The barrel-stave has been primarily used for underwater sonar applications and thus can be used in a fluid-filled borehole as well as within a fluid-filled inflatable canister like that used to house the piezocylinders.

- For a receiver array, we have developed an inflatable membrane system for coupling uniaxial or triaxial accelerometers to the wall of an open borehole.

5.1.2 Inversion Software

- An analysis software was developed to create an image of the material adjacent to the borehole based on full wave inversion (FWI) technology.
- To perform FWI for this application, the cylindrical geometry and the associated boundary conditions must be modeled correctly.
- Due to the formidable computer time of 3D borehole inversion, an ABAQUS-based axisymmetric forward model was chosen for the proposed imaging effort.
- The inversion was based on a regularized Gauss-Newton method implemented in MATLAB and the interface between ABAQUS and MATLAB was developed using Python script.
- The system can be run within the Student Version of ABAQUS, which is available for no cost.

5.1.3 Validation Experiments

- Experiments in an acrylic tube borehole model demonstrated that the piezocylinder source and amplifier can generate enough energy at high frequencies to be effectively measured by our inflatable membrane accelerometer receiver array. This experiment demonstrated the basic concept of a moveable and repeatable system for generating and measuring a wavefield within a borehole.
- Experiments in a cylindrical borehole model constructed from synthetic limerock demonstrated that the system concept does work with a more realistic material (limerock rather than acrylic). The cylindrical model experiments also demonstrated an effective inflatable canister for repeatable coupling of a piezoelectric cylinder source in a borehole.
- Experiments on the top flat surface of a cubical synthetic limerock model with borehole were used to learn how to process full waveform records for use in the inversion software, including choice of motion component to invert (i.e., acceleration, velocity, or displacement) and types of temporal and frequency filtering.
- Experiments using the PVC-cased boreholes at the Newberry field site demonstrated that the

low frequency pneumatic solenoid source can produce a wavefield that can be measured throughout the length of the 3D geophone array. This was our first field implementation of generating a wavefield using a source and receiver array from within a single borehole.

- Experiments using the PVC-cased boreholes at the Newberry field site demonstrated that the barrel stave source with the 3D geophone string do not work well together as currently configured. The high-voltage signal sent to the source is coupled to the unshielded cable for the geophones. The coupled signal is large and completely masks any of the signal transmitted by the geophones when mechanically shaken. However, a measurable mechanical vibration was registered by an accelerometer mounted to the top of the PVC casing.

5.2 Conclusions

Based on the findings outlined above, the following conclusions are drawn:

- It has been demonstrated via both the piezoelectric and pneumatic solenoid sources and the accelerometer and geophone arrays that wavefields can be generated and measurably received within a single borehole.
- It has been demonstrated via synthetically generated waveforms that a full waveform-based analysis software can image the material surrounding a borehole.

5.3 Recommendations

The following recommendations are suggested after reviewing all of the findings and conclusions discussed above:

- We have developed a working concept for a borehole instrument and analysis software for geophysical assessment of the material surrounding a geotechnical borehole. Further tests are warranted to help validate the new procedure. As well, some additional details are recommended for improving the instrumentation described herein.
- The barrel stave source currently works in a fluid-filled borehole, but an inflatable bladder system for repeatable coupling of the source in a dry borehole should be developed.
- For potential use with the barrel stave source, a better system for shielding the 3D geophone string should be developed to at least demonstrate whether or not these geophones can effectively measure the waveforms generated by this source.

- For generating a low frequency wavefield around a borehole that can be effectively measured with the 3D geophone string, modifications should be made to the pneumatic solenoid source to relieve crowding.
- Conduct additional model and field experiments to demonstrate effectiveness of the proposed changes listed above and to generate real experimental data for trials with the inversion software.

LIST OF REFERENCES

ABAQUS (2013), *ABAQUS Analysis User's Manual*, Version 6.13, Habbit, Karlsson and Sorenson, Inc, Pawtucket, RI.

Aster, R. C., Borchers, B., and Thurber, C. H. (2005). *Parameter Estimation and Inverse Problems*. Academic Press, Waltham, MA.

Bunks, C., Saleck, F. M., Zaleski, S., and Chavent, G. (1995). "Multiscale seismic waveform inversion." *Geophysics*, 60(5), 1457-1473.

Hiltunen, D.R. and Jiang, P. (2013), "Continuation of Down-Hole Geophysical Testing for Rock Sockets," *Final Report for Contract BDK-75-977-51*, Florida Department of Transportation, November, 118 pp.

Kalinski, M.E. (2012), "A Small, Lightweight Borehole Receiver for Crosshole and Downhole Seismic Testing," *Geotechnical Testing Journal*, ASTM, Vol.35, No. 2, 4 pp.

Sheen, D. H., K. Tuncay, C. E. Baag, and P. J. Ortoleva, Time Domain Gauss–Newton Seismic Waveform Inversion in Elastic Media, *Geophysical Journal International*, Vol. 167, No. 3, 2006, pp. 1373–1384.

Sirgue, L. and Pratt, R. G. (2004). "Efficient waveform inversion and imaging: A strategy for selecting temporal frequencies." *Geophysics*, 69(1), 231-248.

Thill, R.E. (1978), "Acoustic Cross-Borehole Apparatus for Determining In Situ Elastic Properties and Structural Integrity of Rock Masses," *Proceedings of 19th U.S. Symposium on Rock Mechanics*, Reno, NV, May 1-3, pp. 121-129.